UNIVERSITAT POLITÈCNICA DE VALÈNCIA

ETS INGENIERÍA DE CAMINOS, CANALES Y PUERTOS

TRABAJO DE FIN DE GRADO

Numerical Wave modeling Analysis in the port of Barcelona with REEF3D.

Presentado por

Arnau Landaluce, Pablo Martin

Para la obtención del

Grado en Ingeniería Civil

Curso: *2020/2021*

Fecha: *14/09/2021*

Tutor: *Maria Esther Gomez Martin*

Cotutor: *Weizhi Wang*

Numerical wave modeling analysis in the port of Barcelona with REEF3D

A Bachelor Thesis
submitted to the Department of Civil and Environmental Engineering
at the Norwegian University of Science and Technology

Civil Engineering

by

Pablo M. Arnau Landaluce

Abstract

Ports are currently one of the main infrastructures for managing global trade. Currently more than 80 per cent of the world's goods traded by volume is transported by sea due to its low costs. Thus making maritime transportation the back bone of globalized trade and supply chain. Consequently , the majority of manufacturing and production plants in the world have been located near the coast with good access to a commercial port. Being one of the main factors of the general transportation sector and a key factor on the logistics supply chain, their activity have direct influence on global economic development.
The design and construction of ports imply a great economic importance as they are they are extremely pricey. To reduce uncertainty while designing and constructing their infrastructure both physical and numerical models are used. These allow to test and modify designs in order to improve efficiency and reduce negative economic, social and environmental impact. Accurate numerical models provide a desirable wave forecast and can prevent several disasters during the construction and exploitation of harbors. Phase-resolved numerical models provide a reliable representation of the wave field over time. The goal of the study is to analyze wave propagation and transformation in the Barcelona harbor, where a new dock has been projected.

The numerical wave model chosen for this thesis is the phase-resolving model REEF3D ::FNPF. Several simulations were carried out to ensure a proper representation of the wave transformation phenomena. Convergence studies were made in order to select an effective and efficient cell size for the numerical domain. After determining the cell size, three simulations were made with different significant wave heights and peak periods to ensure concurrent results. To select the most unfavorable scenario, the maximum annual significant wave height was selected in the most unfavorable direction for the area regarding the new dock, the southeastern incident waves.

The analysis of wave conditions at the harbor show that strong wave transformation phenomena take place. Thanks to the visual representation of the wave field these phenomena can be observed and studied. This together with the speed and accuracy obtained in the results, make REEF3D::FNPF a great tool for harbor modeling. The

strong diffraction and energy dissipation in the southern entrance of the Barcelona harbor make possible the introduction of a new dock, as they significantly reduce the significant wave height and the spectral energy density.

Acknowledgments

First of all I would like to thank my family for their unconditional support, in particular to my parents. They have supported and helped me for my entire life.

I thank Prof. Hans Bihs for allowing me to develop my thesis with REEF3D, a program that I believe has a lot of potential for the design and analysis of coastal and offshore structures. As well as Dr. Weizhi Wang for his support and help during the development of the thesis.

Lastly I would like to thank my friends from Sjøskrenten for all of the study gatherings on Fridays even though I was tired they made push through it.

Contents

List of Figures

Chapter 1

Introduction

1.1 Harbors and Society

The transportation sector has a great influence in the economic growth and development of a country and its integration in the world's economy. Lower transport costs lead to an increase in exports, lower unemployment rates, higher savings ratio, higher levels of foreign investment and increased access to technology. Therefore, transport costs are key for economic development [20].
Since the world trade organization's agreements begging in the 1980s many international barriers have been lifted and we have grown into the era of globalization. Most multinational companies have re-located their manufacturing plants to developing countries in search of cheap labor force to reduce production costs. Although this is ethically questionable it has lead to the economic growth of several countries like China, India or Taiwan. The current allocation of production has lead to a dramatic increase in the demand of transport.
Currently more than 80 per cent of the world's goods traded by volume is transported by sea due to its low costs. Maritime transportation is the cheapest and most efficient system considering load or volume carried compared to other means of long distance transportation [20]. In 2019 the total world fleet had a 1.97 billion dead-weight tons of capacity, counting with 95,402 ships. Thus making maritime transport the backbone of globalized trade and supply chain. (Review of Maritime transport 2019). For this reason, the majority of production and manufacturing plants in the world are located near the coast with good access to a commercial port for importing raw materials and exporting finished goods.

The action of the waves and the wind cause a constant movement of the water level. This movement decreases boats' maneuverability making it challenging also for unloading and loading passengers and cargo. Ports are designed to decrease the wave

height inside their basin in order to ease the docking, loading and unloading of boats for maritime transport of goods or people. The location of ports are chosen to optimize the access to navigable water and land. They may have one or several harbors, which are places where ships seek shelter. They include anchorage spots for boats an structures like, breakwaters, quays, access channels, jetties, landing stages, ship sheds, slipways for ships and storage facilities. Dry ports are a secure inland area for managing temporary storage, custom clearance and inspection of international traded goods. They are a key aspect for the efficient running of ports, providing services for the treatment and provisional storage of cargoes and containers that flow in and out of the port by any transport system such as railways, roads, airports or inland waterways [20].
Ports are currently linked to the growing wold's economy since they are one of the main factors of the general transportation sector. Being a key factor of the logistics supply chain, their activity has direct impact on significant economic variables such as final import prices and export competitiveness, hence influencing the world's economic development [45].
The port of Barcelona is responsible for 6.3 percent of the employment in the region of Catalonia and increase their clients' benefits in almost 23000 million euros. Solely the touristic sector of the port is valued on 22 million euros a day and generates around 100,000 jobs [37].

In the current globalized world, enterprises seek to expand their organizations overseas through an export approach. As a result, the country's GDP is fairly affected by the ability of corporations to globally export their goods and services. This is well known so there has been an increase in competition in the port industry to lower even further transportation costs in order to improve attractiveness as ports of call for shipping companies. The current approach is the expansion of ports as they have been found to be more cost-efficient, considering them an economy of scale. The constant development and improvement of both physical and digital infrastructure is needed to maintain a high level of competence, if not they face the risk of ultimately becoming too inefficient to run. The expansion and development of ports can certainly improve a country's economy by increasing trade activity, supply, lowering unemployment, reduced prices for goods and greater foreign reserves.

1.2 Importance of Numerical Wave Modeling

Models, both physical and numerical, are of significant importance for the design and verification of substantial construction projects which usually have considerable economic, social and environmental impact.

The constant development and improvement of our theoretical knowledge of ocean wave phenomena and numerical modeling techniques jointly with technological improvements have made accurate and efficient complex numerical models possible.

Computational advancements have lead to higher time-efficient modeling. In particular,parallel processing on multi-core computers, which allow the simultaneous solving of several problems, each in one of the processing elements of the computer. Additional cores linearly increase the computational speed and thus the modeling speed for multi-core scalable models. This has raised the attractiveness of numerical modeling and has lead to their development as seen in Chapter 3, Numerical Wave Models [19].

Current development in wave models is turning towards increasing time efficiency instead of trying to accurately model all of the hydrodynamic phenomena possible. As seen per [10], who recently developed the FNPF model, a comparison for the time required for modeling wave propagation over a submerged bar was made between CFD and FNPF achieving spectacular results. The models were run through a 12 core computer lasting for 17 hours with the CFD model while the FNPF model only lasted 170 seconds, around 400 times faster. This model also simulated the propagation of a 2D wave field for a time period of over three hours in 1.13 hours with a 16 core supercomputer, almost three times faster than any physical model.

Numerical models are also used in combination with physical models and field data in order to increase our understanding of fluid dynamics in diverse fields of coastal engineering. For example, in the study of the effects of sea level rise and extreme climatic events due to climate change on coral reef hydrodynamics [39] or in the stability assessment of the Three-Gorges Dam [32].

Accurate numerical wave models can also be helpful for the appropriate design of harbors and coastal and marine infrastructure. As stated before these projects are economically demanding and may produce a great social and environmental impact. A good wave forecast can prevent several disasters during the construction and exploitation of these infrastructure.

1.3 Objectives of the study

The objective of the study is to analyze wave propagation and transformation in Barcelona's harbor. For this, numerical waves propagated from offshore towards the

port of Barcelona, Spain will be computed through REEF3D::FNPF. Results will be analyzed and compared in order to gain a proper understanding of the transformation phenomena of waves entering and propagating throughout the harbor's basin. The study of the wave transformation will mainly focus on the area between the dock "Muelle de la Energía" and the dock "Muelle Prat", where a new dock has been projected. These results and analyses will be considered by the port of Barcelona for the redesign of the new dock.

Chapter 2

Wave Theory

Numerical wave modeling is the practical application of fundamental physical principles. The major fundamental progress on wave modeling has been made in the last 70 years, supported by periods of application and small scale improvements. There are several complex factors to take into account for modeling waves. In order to thoroughly understand and advance in each aspect of wave modeling, researchers focus their investigations in one factor. The constant flow of information between the wave modeling community yields a faster improvement rate, where each researcher or researching team contributes separately with his/her/their own initiatives. Wave generation, non-linear interactions in deep and shallow water, white-capping and the mathematical approach behind these phenomena are the main factors in wave modeling.

2.1 Wind-wave generation

Wind-wave generation is the study of the effects of wind in the water surfaces. It is a complex phenomena to study since it evaluates the interaction between a surface that varies in space and time with the turbulent airflow. It is most important when large scale areas are modeled since there is enough space for the interaction between the wind and the water surface to interact and produce a significant change in the sea state.

The interaction between the wind and the water surface is normally considered through the atmospheric input term of the energy conservation equation in numerical models. The refinement with which the energy transformation has been defined has considerably increased the understanding of the physical processes responsible for wind wave generation. These models are divided as first, second or third generation. The models generated for this thesis incorporate all three, but the second generation model, the JON-SWAP spectrum, will be used, as it considers a constant young sea

state.

$$S_{tot} = S_{in} + S_{ds} + S_{nl} \tag{2.1}$$

Where S_{tot} , the source term, is the total energy, S_{in} is the atmospheric input term, considering it as the normal stress exerted on the water surface. S_{ds}, the dissipation term, is included as a saturation limit to the spectrum. And S_{nl} is the quadruplet nonlinear interaction term [51].

The JONSWAP spectrum model was obtained from the results of the Joint North Sea Wave Project by Hasselmann et al (1973). This study showed the importance of nonlinear quadruplet interactions in the generation and propagation of the wave field.

2.2 Non-linear quadruplet interactions in deep water

The joint North Sea wave project (JONSWAP) proved the importance of the resonant weak nonlinear interactions between groups of four waves in the evolution of the energy spectrum of free surface gravity waves based con Hasselmann's discoveries.
[25] studied the energy flux in the spectrum produced from nonlinear interactions between several wave components. For the perturbation analysis he considered an irrotational ideal fluid with constant water depth. Neglecting surface tension, he was able to determine the velocity potential and the surface fluctuation by setting up a system of equations considering the continuity equation, the kinematic boundary conditions at the bottom and at the free surface, and the dynamic boundary condition. He then used the perturbation functions obtained to determine the energy of the sea in order to analyze the energy transfer between waves.
Hasselmann concluded that a group of four waves could exchange energy in the form that he called quadruple interactions. Energy transfers from three 'active' waves to a fourth 'passive' wave if the following resonant conditions are satisfied:

$$\overrightarrow{k_1} + \overrightarrow{k_2} = \overrightarrow{k_3} + \overrightarrow{k_4} \tag{2.2}$$

$$\omega_1 + \omega_2 = \omega_3 + \omega_4 \tag{2.3}$$

Where k_i is the wave number and ω_i is the angular frequency. For deep water conditions the linear dispersion relation, which relates the angular frequency to the wave

number is simplified as:

$$\omega^2 = g * k \tag{2.4}$$

Where g is the acceleration due to gravity.

Hasselmann formulated the quadruple interactions in the terms of their action density as:

$$\begin{aligned}\frac{\partial \eta_1}{\partial t} = \int\int\int G(\overrightarrow{k_1}, \overrightarrow{k_2}, \overrightarrow{k_3}, \overrightarrow{k_4}) * \delta(\overrightarrow{k_1} + \overrightarrow{k_2} - \overrightarrow{k_3} - \overrightarrow{k_4}) * \delta(\omega_1 + \omega_2 - \omega_3 - \omega_4) \\ * [\eta_1\eta_2(\eta_3 + \eta_4) - (\eta_1 + \eta_2)\eta_3\eta_4] d\overrightarrow{k_2} d\overrightarrow{k_3} dk_4\end{aligned} \tag{2.5}$$

Where $\eta_i = \eta(\overrightarrow{k_i})$ is the action density at wave number $\overrightarrow{k_i}$, $\eta(\overrightarrow{k}) = E(\overrightarrow{k})/\omega$, E is the energy density, G is the coupling coefficient, and δ are functions that assure that the integral's inputs are solely from quadruplets that satisfy the resonant conditions, establishing the conservation of wave momentum, wave action and wave energy.

The energy flux tend to redistribute the energy in a relative uniform manner over all wave numbers, tending to reduce sharp peaks in the spectrum. Thus, at the initial period of development of wind-generated sea waves, the energy would transfer from high to low wave numbers and in the opposite direction, from low to high wave numbers, when the energy is concentrated in the low wave numbers [25] [14].

2.3 Spectral Dissipation in deep water

Represented by S_ds in the source term, the dissipation phenomena is the loss o energy in the wave spectrum. It is the most unexplained physical phenomena of wave modeling. The major factor affecting the dissipation of energy is assumed to be the wave breaking, followed by wave-turbulence interaction and wave-wave modulation.

Several models have been made trying to define the spectral dissipation due to wave breaking, such as quasi-saturated models, probability models, turbulent models and whitecap models, this final one is the most commonly used. However, the physics behind wave breaking is still unclear.

Whitecapping is essentially wave breaking in deep water. Also known as steepness induced wave breaking, this phenomenon occurs when the wave steepness, which is the relationship between the wave height and wavelength, overpasses a certain threshold

value, which produces an instability in the wave an causes the wave to break. Whitecaps models have two approaches, the after-breaking class model and the pre-breaking model. The after-breaking class model, introduced by [26], is the most common dissipation model used. This model is based on the random distribution of white caps on the front of breaking waves. The whitecaps apply pressure on an ascending wave producing a linear dissipation. Nonetheless, two essential assumptions are made that are lacking experimental verification, a weak dissipation around the mean and a geometric similarity between whitecaps and sea waves [14].

2.4 Non-linear interaction in Shallow water

As wave propagate from deep to shallow water the dispersion relation changes from a dispersive deep water regime to a non-dispersive shallow regime where the speed becomes equal throughout all the wave components. This produces the shift between quadruplet interactions to triad interactions between waves, making the triad interaction the major factor of non-linear transformation of irregular surface gravity waves. The triad wave-wave interaction is the energy flux from the incident wave components to lower and higher frequency components [14] [33]. These interactions can occur when the following conditions are satisfied:

$$f_1 \pm f_2 = f_3 k_1 \pm k_2 = k_3 \tag{2.6}$$

Where f is the frequency and k is the wave number. The components 1 and 2 must also satisfy the linear dispersion relationship.

$$\omega^2 = gktanh(kh) \tag{2.7}$$

Where ω is the angular frequency, g the acceleration due to gravity and h the water depth.

Non-resonant interactions take place in intermediate water depths when the third component doesn't satisfy the dispersion relation, resulting in small amplitude bound harmonics. Whereas resonant interactions take place only in really shallow waters when the third wave component satisfies the dispersion relation, resulting in an increase of its amplitude [21]. This interactions widen the frequency wave spectrum and phase-couple the spectral components in shallow water, provoking a forward pitching and steepening of near-breaking wave crests.

When waves near shore reach a certain amplitude to water depth ratio they break,

rapidly transforming from an oscillatory, sinusoidal, state of propagation into a turbulent state with high kinetic energy and then back to a lower energy oscillatory state.

The first numerical parametrization of breaking waves, developed by Irribarren and Nogales (1949)[27] was through what is known as the Irribarren number:

$$I = \frac{m}{(H/L)^{1/2}} \tag{2.8}$$

Where m is the slope, H originally was the wave height in an offshore point and L the wave length in the same point offshore. However, currently the Irribarren number is defined with H and L at the breaking point.

Galvin (1968) [24] classified the breaking waves considering their visual characteristics:
Spilling breakers, $I < 0.6$, when breaking waves have an initial white water at the wave crest and then spreads down the front face. These usually take place in beaches with low or no slope.

Plunging breakers, $0.6 < I < 2.0$, the typical waves for surfing, normally occur on medium to steep sloped beaches. The wave crest curls over the wave, enclosing a body of air when it plunges in front of the wave into the water, creating a lot of bubbles and turbulence.

Surging breakers, $I > 2.0$, this type of breaking waves occur on steep sloped beaches, where waves usually break sliding up the shore producing a small amount of bubbles.

For coastal engineering designs the two main aspects studied in breaking waves are the wave height and the energy dissipation. In shallow water the breaking height is determined by the water depth, where waves, in a simplified manner, start to break when the wave height to water depth ratio is around 0.78. The mathematical approach for wave breaking is described in the numerical model 3.4 [42].

2.5 Bottom Dissipation

As waves advance into shallow water they start interacting with the sea bed. Here white-capping, nonlinear energy transfer and wind input interact differently due to the depth limited conditions. There is some strong evidence about the necessity of wave-bottom interaction to complete the energy balance in shallow water. Several factors are known to cause energy dissipation, such as bottom friction, percolation into porous media, bottom roughness, soft mud, bed motion and turbulent bed shear

stress.

Bottom friction produces an energy dissipation on a similar order of magnitude as the energy input from moderate winds. Its energy dissipation is directly proportional to the bottom shear stress and to the orbital velocity of the wave. The bottom friction has been studied through two main approaches, considering only the wave-bottom interactions and considering the joint interactions between currents and waves with the bottom stress.

In coastal areas with sandy bottoms, sediment transport due to the bottom friction plays an important role on the energy dissipation. When sediment transport occurs, some the energy in the water is passed on to the sand grains as kinetic energy as they move. For taking it in consideration, the bottom roughness has to be characterized. It is usually parametrized by the grain size and on the current and past hydrodinamic conditions. [14].

Chapter 3

Numerical Wave Models

Free surface elevation, diffraction, refraction, wave shoaling and several other physical processes of waves are of significant importance for the design of coastal and marine structures. Technological advancements have encouraged the development and use of several numerical models, which nowadays are found to be cost effective and very reliable for solving coastal engineering problems.

Chalikov defines mathematical modeling as "a method of investigation of complicated processes based on a full mathematical formulation of a problem" [16]. Models are generally classified as phase resolving models or phase averaging models.

3.1 Phase-averaged wave modeling

Phase averaging models forecast average or integral parameters of the wave field. These may be significant wave height, peak period, temporal and spatial evolution of the directional spectrum, etc. These models solve one equation, which simplifies for deep water as the following 3.1:

$$\frac{\partial F}{\partial t} + C_g \cdot \nabla F = S_{tot} \tag{3.1}$$

Where C_g is group velocity vector, and $F = F(f, \Theta, x, y, t)$ is the directional spectrum [51].

3.1.1 Spectral Wave Models

In Spectral wave models waves are considered as density of potential energy as a function of frequency, time, direction and physical coordinates [15]. These models

are able to simulate wind generated wave fields over large offshore ocean areas with coarse grids in a really computational efficient and effective manner. However they have limited capabilities simulating complex coastlines and near shore areas due to their limiting capacity of defining nonlinear phenomena such as reflection, wave breaking and strong diffraction. Consequently these models are often used for obtaining realistic input waves for phase-resolving modeling, where the waves are simulated from offshore to near shore with phase-averaging spectral models and phase-resolving models are used to forecast wave phenomena in complex coastlines and coastal structures [48].
For this project the well-known spectral wave model SWAN will be used to simulate offshore waves in order to have reliable data input for the two phase-resolving models that will be used for modeling the harbors. Swan is a third-generation spectral wave model mainly designed for obtaining accurate values for wave parameters for the transition from ocean ranges to coastal areas. [12]. It is able to consider several key physical processes specific to deep water and also to transition and shallow water essentially reflections, shoaling, triad wave-wave interactions, refraction, depth-induced breaking, bottom friction, energy from the wind, quadruplet wave-wave interactions and white capping.
SWAN solves the energy conservation equation 3.2 that describes the temporal and spatial evolution of the wave spectrum:

$$\frac{\partial N}{\partial t} + \nabla[(\overrightarrow{C_g} + \overrightarrow{U})N] + \frac{\partial C_\sigma N}{\partial \sigma} + \frac{\partial C_\theta N}{\partial \theta} = \frac{S}{\sigma'} \tag{3.2}$$

where t is time, S, the source term, is energy density, θ is the direction of the waves, σ is the relative frequency, N is the energy spectrum to relative frequency ratio, $\overrightarrow{U}$ is the velocity of the current, and $\overrightarrow{C_g}$ is the group velocity ($\overrightarrow{C_g} = \frac{\partial \sigma}{\partial \overrightarrow{k}}$), where k is the wave number, $C_\theta = \theta$ and $C_\sigma = \sigma$ for the spectral space. [40]

3.2 Phase-resolving wave modeling

Phase resolving models are able to predict the phase and amplitude of individual waves, therefore capturing diffraction and other nonlinear interactions much better than phase averaged models. This makes them much more computationally demanding than phase averaged models, consequently, their domain of application is usually restricted to complex coastlines and wave-structure interaction, where they are strictly needed.

3.2.1 Shallow water wave models

Shallow water equations can be applied in a large range of engineering cases such as rivers, open channels, flood, tsunami and coastal modeling by deriving the conservation of mass and momentum from the Navier-Stokes equations considering the region of study as shallow water. Shallow water is considered when the bottom topography has an influence on the evolution of free surface waves, this depth is relative to the wave length being considered when $h/L \leq 0.05$. Where h is the water depth and L is the wave length. Even though they are widely applied for modeling the fact that shallow water has to be assumed limits its use in open waters.

When dealing with small wavelengths or rapidly varying bathymetry the effects of the non-hydrostatic pressure cannot be neglected anymore, thus dispersion has to be included into the flow motion. There are two main models for this, the Boussinesq model and the non-hydrostatic model.

Non-hydrostatic wave models

The non-hydrostatic approach for shallow water equations is based in the solution of the incompressible Navier-Stokes equation, considering an inviscid fluid and assuming shallow water. For the application of the non-hydrostatic approach for shallow water equations the pressure is divided into non-hydrostatic and hydrostatic components. Hydrostatic pressure is referred to the pressure produced by the water column over a point, while the non-hydrostatic pressure is the pressure exerted by the rotational movement of the water particles. The projection method is used for solving the time-discretized Navier-Stokes equations through a finite-difference method [17]. The momentum is first calculated as incompressible and then corrected by the solution of a Poisson to obtain the real pressure. [29].

In order to accomplish equivalence between the non-hydrostatic and the Boussinesq model, Jeschke et al. [29] introduced a quadratic vertical non-hydrostatic pressure profile. It was presented as an interesting alternative as it could avoid the numerical instabilities due to high order terms in a boussinesq-type model.

This lead to the development of REEF3D:SFLOW . "The first non-hydrostatic shallow water model with high order discretization schemes" [49]. The high order numerical methods gave the model the ability to represent non-linear long wave propagation over irregular bathymetry, as well as wave-structure interactions. For wave generation and absorption SFLOW applies the relaxation method presented by Jacobsen et al (2012). This method is based on the Reynolds averaged Navier-Stokes equations coupled with the continuity equation for incompressible flows [29]. Waves are generated within a wavelength without any perturbation in a relaxation zone. To prevent the disturbance of the generated waves the waves that are reflected back towards the inlet are absorbed. At the outlet, waves are dissipated to prevent negative impacts

in results due to reflection. Numerical values for horizontal and vertical velocities are gradually decreased to zero, the pressure is lowered to the hydrostatic distribution for the still water level and the free surface is reduced to the still water level in the numerical beach relaxation zone. Therefore reflections are avoided and the energy is absorbed correctly. This model will be thoroughly explained in chapter 3.4 [6].
In addition, WANG et al. also presented a good scalability up to multi-hundreds of processors by using a Message Passing Interface (MPI), which increased dramatically the efficiency and the range of the model [49] .

3.2.2 Potential Flow wave models

These models are based on the Laplace equation,presented in equation 3.4 obtained from neglecting viscosity and assuming an irrotational flow in the Navier-Stokes equation, this way a potential-flow problem is obtained [11].

$$\frac{\partial^2 \phi}{\partial x^2} + \frac{\partial^2 \phi}{\partial y^2} + \frac{\partial^2 \phi}{\partial z^2} = 0. \tag{3.3}$$

Where ϕ is the velocity potential.

There are different approaches to solve this equation. The Boundary Element Method (BEM)transforms the elliptic solution of the Laplace equation into a boundary integrated equation, hence, reducing the total of unknown variables considerably. BEM has been commonly used to solve wave propagation over a steep slope sea bottom, over a submerged break water and for wave-structure interaction as well as other coastal engineering problems. Nonetheless it is not used over large areas for water wave propagation due to its high computational demands [31].

The approach used in this thesis is the finite difference method together with the kinematic, dynamic and bottom boundary conditions, also known as the finite difference potential flow model. Here the Laplace equation is solved by a multigrid method [13] this way fewer calculations have to be made (compared to BEM), making it one of the best numerical solving methods. Fewer calculations result in a smaller computational power required, making it suitable for its application in a 3D model over a large area [31].

In order to include the sea bed boundary a $\sigma - coordinate$ transformation is normally used. By using a non-uniform grid spacing and allowing the clustering of grid points a higher resolution and accuracy is obtained without increasing the computational power required. A 5th order weighted essentially non-oscillatory finite difference scheme is used for the spatial discretization allowing the representation of

extreme changes in bathymetry, maintaining the balance between stability, accuracy and efficiency [30]. High-order Ruge-Kutta schemes are the preferred method for the time discretization as a means to an accurate definition of the non-linear phenomena. Hence wave diffraction, reflection and nonlinear wave effects are all considered automatically [11]. The arbitrary bottom topography enables a fully nonlinear analysis of potential flow up to the point of wave breaking over complex coastal areas [22] . A wet-dry algorithm presented by [52] together with the level-set method presented by (Osher and Sethian (1988)) [35] are used for defining an irregular coastline while maintaining a uniform structured grid over a complex topography. In the model waves can be generated through the Relaxation method, the Neumann boundary conditions or through wave maker motion(piston-type, flap-type, double-hinge) and viscous damping is generally used for wave breaking [8].

3.3 REEF3D

Both of the phase resolving wave models described before are part of the open source hydrodynamic software REEF3D [7]. REEF3D is designed for modeling hydraulic, coastal and marine engineering problems. The software contains four main modules each focused in different areas of study. The CFD module is a complex fluid dynamics model which is able to capture the wave-structure interactions [1], [2], [3], the SFLOW module [50] is ideal for near-shore hydrodinamic modeling, and the FNPF model [9] can be used for large-scale phase-resolved ocean modeling at all depths.

3.4 REEF3D::FNPF

3.4.1 Validated Cases

FNPF has been validated through several benchmark cases which have demonstrated its ability to properly simulate irregular wave fields capturing nonlinear phenomena even in large-scale areas.

In terms of regular wave propagation the model has been validated through several wave theories such as the modeling of linear waves through a constant intermediate water depth, comparing the simulation of second order Stokes waves over constant water depth in a numerical tank with the experimental case carried out by Onotaro et al. (2005, 2006), and a bi-chromatic wave over rapidly changing steep bathymetry generated by a double-hinged flap wave maker where the wave spectra and free surface elevations simulated where compared to the experimental results obtained by

Pakozdi et al (2019a) [8].

To demonstrate the accurate representation of the shoaling and de-shoaling effects the model was validated by propagating linear and second order stoke waves over a submerged bar where the free surface elevation was plotted over time in different wave gauges comparing the results to those obtain by Beji and Battjes (1993) [5]. The experimental case carried out by Ting and Kirby (1995) [44] simulating wave breaking over a mild slope was also performed with a 5th order Cnoidal wave generated using the Neumann boundary conditions. The numerical and experimental results where compared and the study concluded that wave breaking was properly detected and the energy was dissipated accurately.

Several cases where implemented to validate a correct representation of focused waves. The experimental wave packet from the LargeWave Flume (GWK) [18] and the NewWave theory where simulated generating waves with both the Neumann boundary conditions and the relaxation method in order to analyze the effects of wave generation methods. The experimental and mathematical results where compared and two main conclusions where obtained. First, the wave generated through the Neumann boundary conditions focused a higher wave in a further and later position than the LargeWave Flume(GWK) experimental results concluding that the numerical set up calculated the position and timing of the focused waves with higher accuracy than the experimental model thanks to its almost continuous outputs. The second conclusion stated that the relaxation method wave group the focused waves are obtained earlier but over predicting the focusing wave crests. Thus representing less accurately as wave steepness is increased. Therefore the Neumann boundary condition is recommended for the generation of the focusing waves.

In order to validate a correct representation of irregular waves as well as the choice of frequency range, time stepping and grid resolution in the model two main studies where made. First, a three hour irregular wave simulation over constant bathymetry, where the irregular waves were generated by a linear superposition of a finite number of individual regular wave components with different frequencies, amplitudes and phases. The wave spectrum generated was compared to the theoretical spectrum to certify the results. Second a study analyzing four different scenarios with different breaking severity, water depth and wave spectrum was carried out which compares the methodologies regarding the grid resolution, time stepping and frequency range. The scenarios were validated through several mechanisms in order to certify the results. First, studying the kurtosis of the time series at the gauges, checked the quality of the irregular sea reproduction as well as the domain size and the correct location of the gauges. Second, the numerical and theoretical wave spectra were compared

to further validate the irregular sea reproduction. The wave crest distribution was studied to ensure realistic wave crests in the numerical wave field comparing them to the research developed Huand and Zhang (2018)and [23]. This study concluded that the equal energy method (EEM) method leans towards concentrating higher energy near the peak frequency, that the viscous damping algorithm preserves Kurtosis and wave spectrum more stable than the filtering algorithm, as well as good understanding on the domain size, frequency range, horizontal grid size, vertical $\sigma - coordinate$ arrangement and time stepping [8].

The validation for large scale modeling through two main cases, the Mehamn harbor and the Aquaculture site at Flatoya. For the Mehamn harbor an area of 14 by 10 km was represented and took less than 8 hours using 128 cores from the Vilje supercomputer. The case studied the effects of several combination of breakwaters and its effects on wave height, diffraction, refraction and other nonlinear phenomena. The theoretical and produced wave spectra were compared, as well as the free surface elevation in several gauges with the results from physical model carried out by Vold and Lothe (2009) [47]. For the aquaculture site at Flatoya the sea reproduction of 14 by 7 km domain was compared to that produced by SWAN. As expected FNPF represented refraction and other non-linear phenomena much batter than SWAN, obtaining a specific wave height 20 to 50 per cent higher. The studies concluded that the model was ready for large scale engineering scenarios [8] .

3.4.2 Governing equations

The fully nonlinear model's governing equation is the Laplace equation and it solved by considering the kinematic, dynamic and bottom boundary conditions:

$$\frac{\partial^2 \phi}{\partial x^2} + \frac{\partial^2 \phi}{\partial y^2} + \frac{\partial^2 \phi}{\partial z^2} = 0. \tag{3.4}$$

The kinematic, dynamic and bed boundary conditions are required for solving the velocity potential ϕ from this elliptic equation. The dynamic boundary condition, equation 2.x, ensures a constant pressure directly above and below the free surface, while the kinematic boundary condition, equation 2.x, assures that the water particles on the free surface remain at the free surface. The bottom boundary condition, equation 2.x, establishes an impermeable bed assuring that the velocity normal is zero. These assumptions must be satisfied at all times and are mathematically represented as follows:

$$\frac{\partial \eta}{\partial t} = -\frac{\partial \eta}{\partial x}\frac{\partial \widetilde{\phi}}{\partial x} - \frac{\partial \eta}{\partial y}\frac{\partial \widetilde{\phi}}{\partial y} + \widetilde{w}\left(1 + \left(\frac{\partial \eta}{\partial x}\right)^2 + \left(\frac{\partial \eta}{\partial y}\right)^2\right), \tag{3.5}$$

$$\frac{\partial \widetilde{\phi}}{\partial t} = -\frac{1}{2}\left(\left(\frac{\partial \widetilde{\phi}}{\partial x}\right)^2 + \left(\frac{\partial \widetilde{\phi}}{\partial y}\right)^2 - \widetilde{w}^2\left(1 + \left(\frac{\partial \eta}{\partial x}\right)^2 + \left(\frac{\partial \eta}{\partial y}\right)^2\right)\right) - g\eta. \tag{3.6}$$

$$\frac{\partial \phi}{\partial z} + \frac{\partial h}{\partial x}\frac{\partial \phi}{\partial x} + \frac{\partial h}{\partial y}\frac{\partial \phi}{\partial y} = 0, \quad z = -h. \tag{3.7}$$

where η is the free surface elevation, $\widetilde{\phi} = \phi(\mathbf{x}, \eta, t)$ is the velocity potential at the free surface, $\mathbf{x} = (x, y)$ represents the location at the horizontal plane, $\widetilde{w}$ is the vertical velocity at the free surface and $h = h(\mathbf{x})$ is the water depth considered from the still water level (SWL) to the sea bottom.

The σ-coordinate in the vertical axis is used for solving the Laplace equation with the boundary conditions considered. This coordinate system follows the water depth changes and offers flexibility for irregular boundaries. The transformation from a Cartesian grid to a σ-coordinate is expressed as follows:

$$\sigma = \frac{z + h\,(\mathbf{x})}{\eta(\mathbf{x}, t) + h(\mathbf{x})}. \tag{3.8}$$

The velocity potential after the σ-coordinate transformation is denoted as Φ. The boundary conditions and the governing equation in the σ-coordinate are then written in the following format:

$$\Phi = \widetilde{\phi} \qquad , \sigma = 1; \tag{3.9}$$

$$\begin{aligned} &\frac{\partial^2 \Phi}{\partial x^2} + \frac{\partial^2 \Phi}{\partial y^2} + \left(\frac{\partial^2 \sigma}{\partial x^2} + \frac{\partial^2 \sigma}{\partial y^2}\right)\frac{\partial \Phi}{\partial \sigma} + 2\left(\frac{\partial \sigma}{\partial x}\frac{\partial}{\partial x}\left(\frac{\partial \Phi}{\partial \sigma}\right) + \right. \\ &\left.\frac{\partial \sigma}{\partial y}\frac{\partial}{\partial y}\left(\frac{\partial \Phi}{\partial \sigma}\right) + \left(\left(\frac{\partial \sigma}{\partial x}\right)^2 + \left(\frac{\partial \sigma}{\partial y}\right)^2 + \left(\frac{\partial \sigma}{\partial z}\right)^2\right)\frac{\partial^2 \Phi}{\partial \sigma^2} = 0 \quad , 0 \le \sigma < 1; \end{aligned} \tag{3.10}$$

$$\left(\frac{\partial \sigma}{\partial z} + \frac{\partial h}{\partial x}\frac{\partial \sigma}{\partial x} + \frac{\partial h}{\partial y}\frac{\partial \sigma}{\partial y}\right)\frac{\partial \Phi}{\partial \sigma} + \frac{\partial h}{\partial x}\frac{\partial \Phi}{\partial x} + \frac{\partial h}{\partial y}\frac{\partial \Phi}{\partial y} = 0 \qquad , \sigma = 0. \tag{3.11}$$

The velocities can be calculated when the velocity potential Φ is obtained within the σ-domain:

$$u(\mathbf{x}, z) = \frac{\partial \Phi(\mathbf{x}, z)}{\partial x} = \frac{\partial \Phi(\mathbf{x}, \sigma)}{\partial x} + \frac{\partial \sigma}{\partial x}\frac{\partial \Phi(\mathbf{x}, \sigma)}{\partial \sigma}, \tag{3.12}$$

$$v(\mathbf{x}, z) = \frac{\partial \Phi(\mathbf{x}, z)}{\partial y} = \frac{\partial \Phi(\mathbf{x}, \sigma)}{\partial y} + \frac{\partial \sigma}{\partial y}\frac{\partial \Phi(\mathbf{x}, \sigma)}{\partial \sigma}, \tag{3.13}$$

$$w(\mathbf{x}, z) = \frac{\partial \Phi(\mathbf{x}, z)}{\partial z} = \frac{\partial \sigma}{\partial z}\frac{\partial \Phi(\mathbf{x}, \sigma)}{\partial \sigma}. \tag{3.14}$$

3.4.3 Numerical schemes

The σ-coordinate transformed Laplace equation together with the boundary conditions is solved through Hypre. Hypre provides an efficient geometric multi-grid solver with parallelization properties enabling time-efficient large domain simulations with multi-core supercomputer infrastructure [46].

The $5th$-order Hamilton-Jacobi version of the weighted essentially non-oscillatory (WENO) scheme ([30]) is used for the discretization of the gradient terms of the free surface boundary conditions. Higher order spatial discretization enables a higher accuracy of representation as nonlinear effects. It also enables wave modeling through abrupt changing bathymetry as the WENO scheme uses weighed smoothness indicators to prevent numerical instability.

A $3rd$-order total variation diminishing (TVD) Runge-Kutta explicit time scheme [41] is used for time discretization. Which calculates the dynamic pressure and the spatial derivatives three times per time step obtaining convergent results. The Courant-Friedrichs-Lewy (CFL) is used to control an adaptive time stepping condition:

$$\begin{aligned} c_u &= \frac{dx}{\left|max(u_{max}, 1.0\sqrt{9.81 * h_{max}})\right|}, \\ c_v &= \frac{dx}{\left|max(v_{max}, 1.0\sqrt{9.81 * h_{max}})\right|}, \\ c_{tot} &= min(c_u, c_v), \\ dt &= c_{tot} CFL. \end{aligned} \tag{3.15}$$

where u_{max}, v_{max} are the maximum particle velocities in x and y directions at the free surface, h_{max} is the maximum water depth.
The model is fully parallelised following the domain decomposition strategy where ghost cells are used to exchange information between adjacent domains. These ghost

cells are updated with the values from the neighboring processors via Message Passing Interface (MPI). The parallel computation enables the model to simulate large-scale scenarios.

3.4.4 Vertical grid arrangement

In order to reduce the computational costs without compromising the accuracy of the model the vertical coordinates follows a stretching function producing denser grids closer to the free surface as follows:

$$\sigma_i = \frac{\sinh(-\alpha) - \sinh\left(\alpha\left(\frac{i}{N_z} - 1\right)\right)}{\sinh(-\alpha)}, \tag{3.16}$$

where α is the stretching factor, i is the index of the point and N_z is the number of vertical cells.
For an accurate reproduction of the phase information and the dispersion relation for deep water waves there has to be a correct stretching layout. Thus a constant-truncation error method is used in order to avoid the cumulative errors from each iteration.

3.4.5 Wave generation and absorption

For the wave generation and absorption the relaxation method, presented by [34] is used in REEF3D:FNPF. This method separates the numerical wave tank into 3 regions. In the first region waves are created, here the surface elevation η and its velocity potential ϕ are pumped to the theoretical values.

$$\varphi(\widetilde{x})_{relaxed} = \Gamma(\widetilde{x})\varphi_{analytical} + (1 - \Gamma(\widetilde{x})\varphi_{computational} \tag{3.17}$$

$$\Gamma(\widetilde{x}) = 1 - \frac{e^{(\widetilde{x}^{3.5})} - 1}{e - 1} \; for \; \widetilde{x} \in [0; 1] \tag{3.18}$$

where $\widetilde{x}$ is scaled to the length of the relaxation zone, normally of one wave length long. The second zone, also know as the working zone, is where the waves are propagated. The numerical beach is the third zone, normally around two wave lengths long, where the waves are dissipated by gradually reducing the free surface elevation η and its velocity potential to still water level, thus reducing the effects of reflection, through the equation presented by [28]:

$$\varphi(\widetilde{x})_{relaxed} = \Gamma(\widetilde{x})\varphi_{analytical} + (1 - \Gamma(\widetilde{x})\varphi_{computational} \tag{3.19}$$

Waves can also be generated through the Neumann boundary conditions and piston, flap and double-hinge type wave makers.

Irregular Waves

Irregular waves are represented through the superposition of an n number of regular waves. These waves can be linear waves, solitary waves or different order Cnoidal or Stokes waves among others, each generated in the generation zone through the relevant wave theories.

3.4.6 Breaking wave algorithm

REEF3D:FNPF takes into account both depth-induced breaking and steepness-induced breaking. Even though the air-entrapment, wave overturning and wave generated turbulence cannot be represented the integral properties of wave breaking such as energy dissipation and wave height are efficiently captured.

Depth induced wave breaking is represented as per SWASH, (2017). When the free surface vertical velocity exceeds the following value relative to the shallow water celerity the waves break:

$$\frac{\partial \eta}{\partial t} \geq \alpha_s \sqrt{gh}. \tag{3.20}$$

where α has a recommended value of 0.6, as it has been proven to work well for all test cases considered (SWASH, (2017). In order to represent the persistence of wave breaking neighboring grid points are considered substituting the variable α by β, where $\beta = 0.3$ is recommended (SWASH, (2017)). Combined with the conservation of momentum and neglecting the dynamic pressure due to breaking, a correct dissipation of energy is obtained, as well as the asymmetry and wave skewness when breaking [43].

A steepness criterion is introduced for considering deep water steepness-induced breaking:

$$\frac{\partial \eta}{\partial x_i} \geq \beta. \tag{3.21}$$

In order to represent a correct dissipation of energy a viscous damping term is introduced around the breaking zone in the free surface boundary conditions as per Baquet et al. (2017) [4] The free surface boundary conditions Eqn. 3.5 and Eqn. 3.6 change to the following when wave breaking is identified:

$$\frac{\partial \eta}{\partial t} = -\frac{\partial \eta}{\partial x}\frac{\partial \widetilde{\phi}}{\partial x} - \frac{\partial \eta}{\partial y}\frac{\partial \widetilde{\phi}}{\partial y} + \widetilde{w}\left(1 + \left(\frac{\partial \eta}{\partial x}\right)^2 + \left(\frac{\partial \eta}{\partial y}\right)^2\right) + \nu_b\left(\frac{\partial^2 \eta}{\partial x^2} + \frac{\partial^2 \eta}{\partial y^2}\right), \quad (3.22)$$

$$\begin{aligned}\frac{\partial \widetilde{\phi}}{\partial t} = &-\frac{1}{2}\left(\left(\frac{\partial \widetilde{\phi}}{\partial x}\right)^2 + \left(\frac{\partial \widetilde{\phi}}{\partial y}\right)^2 - \widetilde{w}^2\left(1 + \left(\frac{\partial \eta}{\partial x}\right)^2 + \left(\frac{\partial \eta}{\partial y}\right)^2\right)\right) \\ &- g\eta + \nu_b\left(\frac{\partial^2 \widetilde{\phi}}{\partial x^2} + \frac{\partial^2 \widetilde{\phi}}{\partial y^2}\right).\end{aligned} \quad (3.23)$$

where ν_b is the artificial turbulence viscosity. $\nu_b = 1.86$ for deep water while $\nu_b = 0.0055$ for shallow water wave breaking are recommended from tested models compared by Baquet et al. (2017).

A geometric filtering approach can be used in combination with the viscous damping method or on its own in order to consider the energy dissipation in breaking waves. The free surface is smoothed for obtaining the energy dissipation with this approach [8].

3.4.7 Coastline algorithm

The level set method by Sethian and Osher (1998) [35] was initially designed to analyze the motion under a velocity field of a bounded region over space and time. A smooth function $\phi(\vec{x}, t)$ was introduced to represent the boundary where $\phi(\vec{x}, t) = 0$.

In order to apply this technique in REEF3D the wetting-drying algorithm is used. Considering the local water depth h as the sum of the still water level, d, and the free surface elevation, η, a minimum depth threshold value is set, with a default value of 0.00005 m. Computational cells with a local water depth above this threshold value are identified as wet cells, while the cells with a water depth below the threshold value are identified as dry cells.

Once all the cells have been identified, the velocities on the dry cells are set to be zero ($u = 0$, $v = 0$) and are assigned a set value. -1 for dry cells and +1 for wet cells. This way the level-set function can be applied in a 2D domain to capture the coastline, Γ, the following way:

$$\phi(\vec{x},t)\begin{cases} > 0 \; if \; \vec{x} \in wet \; cell \\ = 0 \; if \; \vec{x} \in \Gamma \\ < 0 \; if \; \vec{x} \in dry \; cell \end{cases} \tag{3.24}$$

Maintaining a valid Eikonal equation $|\nabla\phi| = 1$ in the level-set function. To prevent numerical instabilities during the wave run-up and run-down processes in the swash zone, the equation is reinitialized at the beginning of each time step through the Partial Differential Equation (PDE) [36]. The equation is iteratively solved until convergence is reached, defining the exact location of the coastline in the zero-contour of the level-set function.

$$\frac{\partial\phi}{\partial t} + S\left(\phi\right)\left(\left|\frac{\partial\phi}{\partial x_j}\right| - 1\right) = 0 \tag{3.25}$$

where $S(\phi)$ is the smoothed sign function [36].

This method enables the use of an efficient structured horizontally-uniform grid even when considering complex topography. Furthermore, the employment of the relaxation method throughout the near-shore areas prevents numerical instabilities due to extreme wave run-ups at severe shallow water regions.

Chapter 4

Barcelona Harbor Modeling

The study will consist on the wave modeling of the coastal area of Barcelona, Spain, where the waves propagated inward the harbors will be analyzed.

The visual representation of the wave field will be used for the analysis of wave transformation phenomena such as diffraction, refraction and reflection. A good comprehension of the effects of the bathymetry and the port structures on wave propagation can be achieved. Wave height, shoaling and wave breaking will be studied though the analysis of the free surface elevation over space and time. The effects of the current breakwaters will be analyzed through the comparison of the wave spectrum inside and outside the harbor's basin, specifically in the main area of study, where the new dock will be constructed(Barcelona).

4.1 Topography

The port of Barcelona is one of the most important harbors in Spain. It is located in the southern border of the city of Barcelona. The harbor is open to sea swell waves at its eastern border. The water depth contour map and a satellite image from 2021 of the harbor and its surrounding area are shown in figure 4.1 and 4.2.

For the simulations of the harbor the bathymetric data was provided by the port authority of Barcelona and the Spanish Oceanographic Institute (IEO), while the topographic data of the harbor's structures and its surroundings was obtained through a topographic survey on google Earth. The bathymetry of the inner harbor was provided with data every 5 meters, while the coastal bathymetric data provided is every 100 meters.
The topography is arranged so that the principal wave directions are east and south-

Figure 4.1: Satelite image of the Barcelona Port. Obtained from google Earth on June 15th, 2021.

Figure 4.2: Topography of the Barcelona Port. Generated through DiveMesh and visualized through Paraview. Rotated for generating southeastern incident waves from the left boundary. Scale 1:1:10

east, with waves generated from the left boundary of the domain. The numerical domain is 15000 meters north south, 10000 meters east west with a maximum water depth of 405 meters. In order to analyze data from all over the harbor 16 wave gauges

were set in the numerical wave tank. Wave Gauges 1-7 are located on the main area of study, where the new dock is projected. Wave Gauges 8-13 are distributed through the main areas of the inner harbor, and wave gauges 14-16 are located on the southern entrance of the harbor, where the waves will propagate towards the main area of study. Their location can be seen in figure 4.9

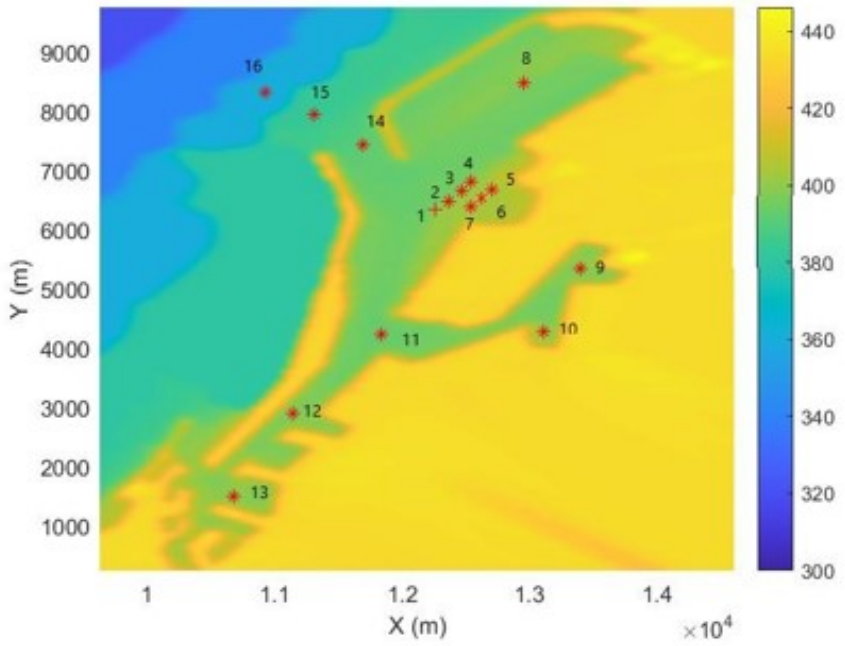

Figure 4.3: Topographic setup rotated for wave generation on the left boundary of the numerical domain. The input bathymetric data was provided by the port authority of Barcelona, IEO and Google Earth.

4.2 Convergence Study

To ensure that the correct cell size is used while running the simulations two convergence studies were run with concurring significant wave height, peak period and direction input values. The 3D convergence study with cell sizes of 40m, 20m, 10m and 8m was conducted. The resulting data was inconclusive and further simulations with thinner grid size is too costly, thus the convergence study was discarded. Furthermore, a 2D convergence study with 20, 10, 8 and 5 m grids was also conducted. From figure 4.4 until the figure 4.6 we can observe that an 8m cell size is optimal for the simulations, since it is the coarsest grid that provides accurate results. From figures 4.4 to 4.6 we can also observe that the effects of the port structures are not taken into account. We can see this by comparing the maximum spectral density from

2D simulations with 3D simulations at each wave gauge. Figures on the appendix .

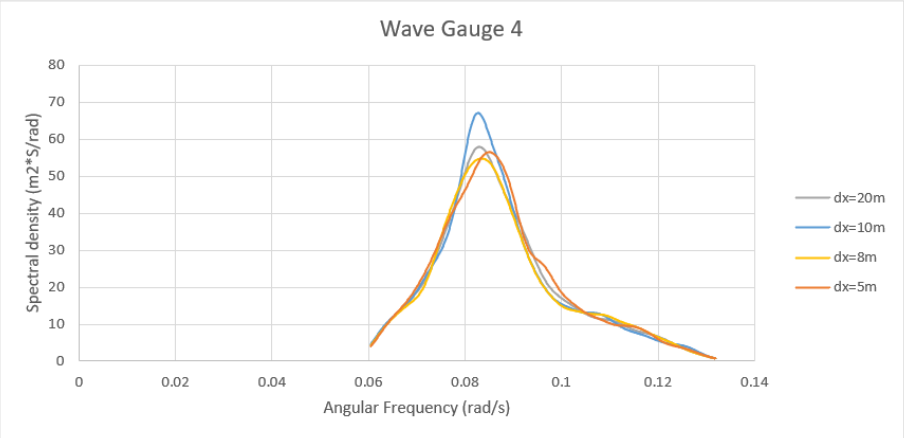

Figure 4.4: Spectrum Comparison 2D convergence study, wave gauge 4

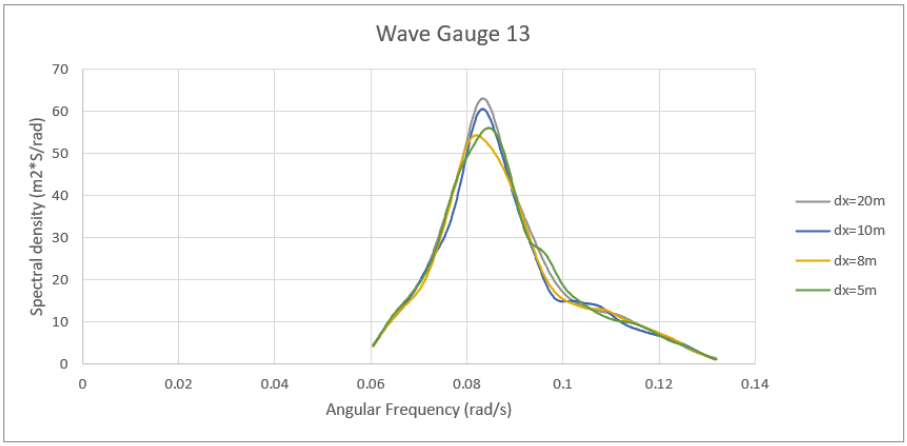

Figure 4.5: Spectrum Comparison 2D convergence study, wave gauge 13

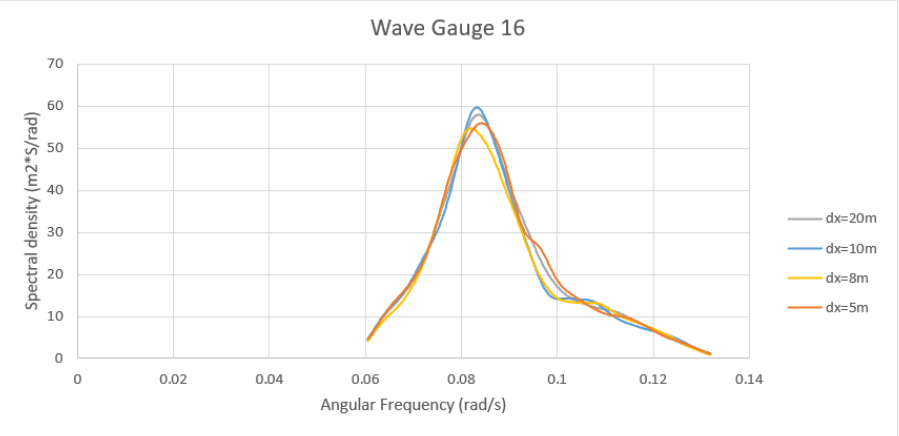

Figure 4.6: Spectrum Comparison 2D convergence study, wave gauge 16

4.3 Simulations

4.3.1 Setup

In order to select realistic values of Hs and Tp of unfavorable scenarios a study with three different Hs and Tp combinations were made.

Different annual maximum significant wave heights and peak periods were simulated in order to obtain the most unfavorable scenarios. The following input data was obtained from the buoy information at [38]. The input spectrum used for the simulation of the sea state is the JONSWAP spectrum with a peak enhancement parameter 3.0. Frequency between 0.05 times peak period and 2 times the peak period, as default values in REEF3D, in order to consider a wide range spectrum on which to work on for reliable results. Wave relaxation zone 250 meters and wave generation zone 250 meters. For the generation of 1st order irregular waves 1024 waves were superpositioned. In order to maintain a reasonable continuity on the report only the results of the 5th simulation will be presented, while the rest of the results will be attached in the appendix. For this simulation a significant wave height of 4.5 meters and a peak period of 11 seconds, with incident waves from the south-east direction, which are the most relevant for the southern entrance and the main focused area.
The generated wave tank consisted of 10 cells in the vertical arrangement, with a stretching factor of 2.0, and 1875-1250 cells in the horizontal plane. 12800 s simulations are performed in order to have enough time for the generation and analysis of the simulated sea state across the whole domain. The surface elevation time histories are used to calculate wave spectra.
With a cell size of 8 m in the horizontal direction and 10 cells in the vertical direction,

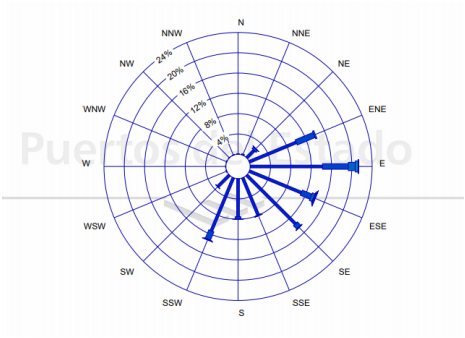

Figure 4.7: Information obtained from the Buoy of Barcelona II report on historical data [38].

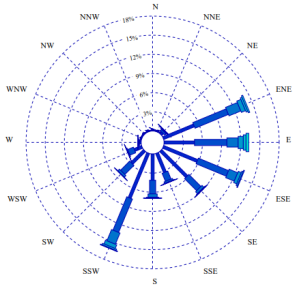

Figure 4.8: Information obtained from the SIMAR point 2110135 report on historical data [38].

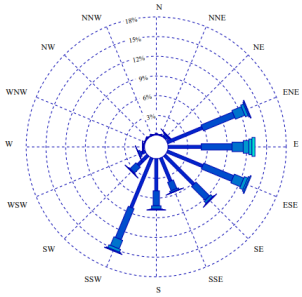

Figure 4.9: Information obtained from the SIMAR point 2111136 report on historical data [38].

the total number of cells is 23,437,500 for the full-scale Barcelona simulation. The directions, significant height and peak period can be seen in figure 4.10

Simulation	Direction	Hs (m)	Tp (s)	Simulation Time (s)
1	SE	5.21	12	47923.4
2	SE	4.5	11	47773.6
3	SE	5	10	48579

Figure 4.10: Directions, Hs, Tp and time taken for the simulations

4.3.2 Results

Since a phase-resolving model was used for the simulation of the sea state the free surface elevation can be reconstructed for the analysis of visual physical phenomena such as diffraction and reflection. This has been done through Paraview, an open-source platform for data analysis and visualization. Since consistent results have been obtained throughout the different simulations only the results from one simulation are presented on this section for maintaining a fluent continuity, while the rest can be seen on appendix.

Figure 4.11: Simulation 2, wave propagation from the south-east direction into Barcelona harbor, Hs=4.5 m , Tp=11 s. Free Surface Reconstruction at t=450s, generating waves at the left boundary.

The coastal zone of Barcelona is mainly exposed to swell waves from the eastern direction, thus the port's protection infrastructure is mainly design to protect from these waves. The southern entrance is designed in such manner that boats enter from the southeast direction, therefore making the harbor most vulnerable to waves in this specific direction. The simulations where consequently made on this direction for analyzing the most unfavorable scenario the harbor can experience. On figure 4.12 diffraction of waves due to the breakwaters can clearly be seen in the southern entrance of the harbor. The wave energy is dissipated and redistributed along the wave front throughout the port's basin. On the simulation videos reflected waves can

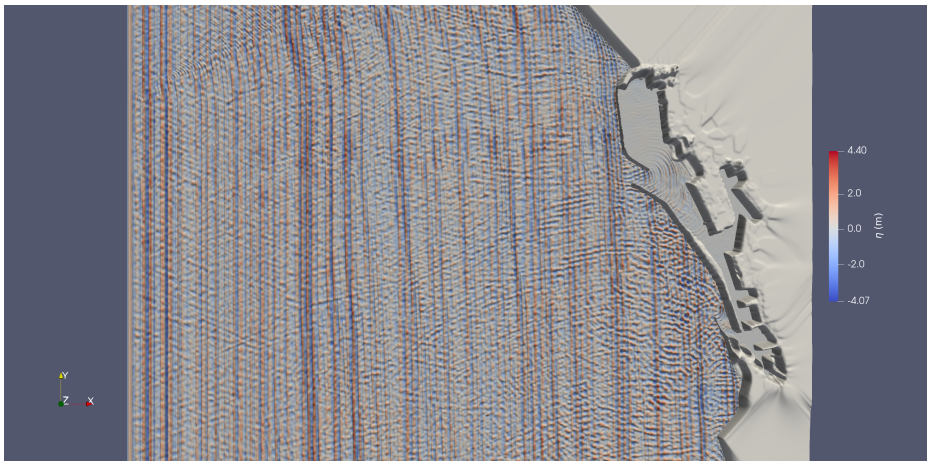

Figure 4.12: Simulation 2, wave propagation from the south-east direction into Barcelona harbor, Hs=4.5 m , Tp=11 s. Free surface reconstruction of young sea state at t=1140s focused on the inner port.

also be seen on the southern end of the basin as well as on the southern corner of the "Muelle de la Energía". These reflected waves disrupt the spectral energy distribution creating two main peaks of energy in the spectrum.
In figure 4.13 we can observe an increase in the maximum spectral density due to the concentration of energy towards the peak frequency from wave gauges 16 to 14 as the southern entrance of the port canalizes the waves towards the harbor. We can also observe the shoaling phenomenon as wave height increase from wave gauge 16 to wave gauge 14 in figure 4.16. The energy is properly dissipated as the spectral energy density is reduced from a maximum of $75.5m^2/Hz$ on wave gauge 14 to a maximum of $10.7m^2/Hz$ inside the harbor on wave gauge 3.

In figure 4.16 the shoaling effect can be observed at the harbors' southern entrance with an increase of significant wave height from 3.97 meters at wave gauge 16 to 4.52 meters at wave gauge 14. A reduction of significant wave height can clearly be seen as the waves propagate from the entrance of the harbor toward the inside. Even though the area where the new dock is projected is the area with the highest significant wave heights. Close to the location of the projected dock,in wave gauges 5,6 and 7, we can observe a maximum significant wave height of 1.16 meters, which should be considered on the design of the new dock.

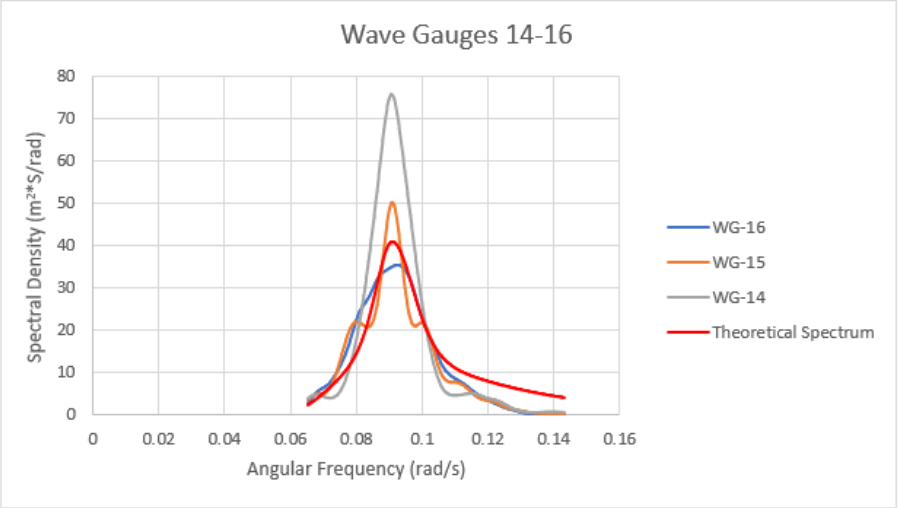

Figure 4.13: Simulation 2, wave propagation from the south-east direction into Barcelona harbor, Hs=4.5 m , Tp=11 s. Spectrum comparison at the southern entrance, wave gauges 16, 15 and 14.

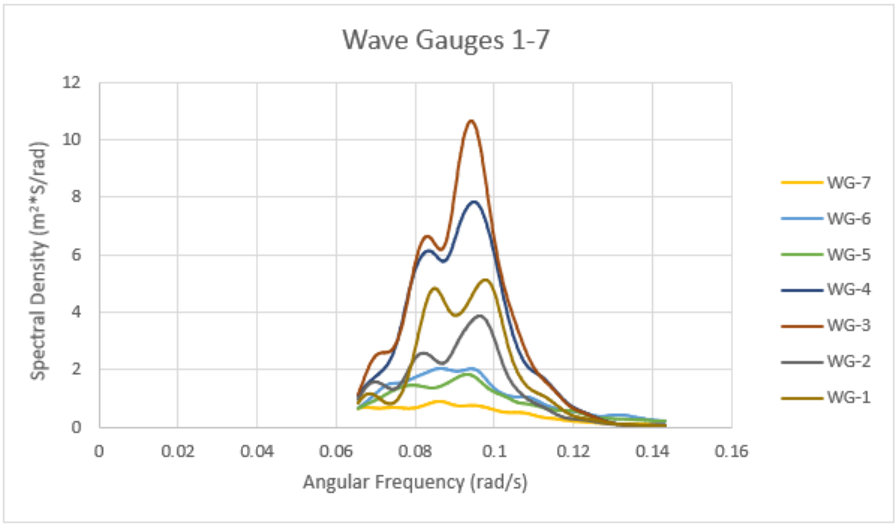

Figure 4.14: Simulation 2, wave propagation from the south-east direction into Barcelona harbor, Hs=4.5 m , Tp=11 s. Spectrum comparison at the main area of focus, where the new dock has been projected.

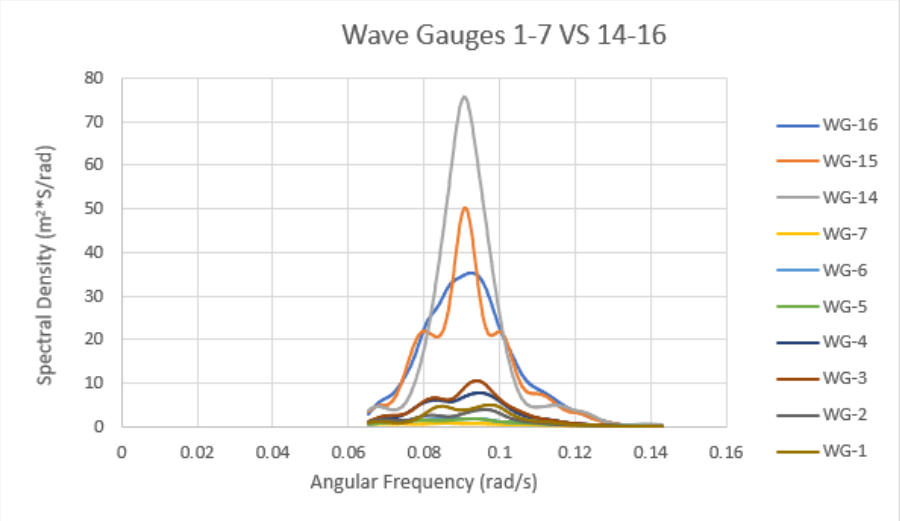

Figure 4.15: Simulation 2, wave propagation from the south-east direction into Barcelona harbor, Hs=4.5 m , Tp=11 s. Spectrum comparison, southern entrance vs. main area of focus.

SE_2			
Location	WG	Hs	Tp
Southern Entrance	16	3.9791	10.8869
	15	3.9096	11.0995
	14	4.5173	10.4955
Area of Focus	1	1.5031	10.4955
	2	1.2927	257.139
	3	2.0371	10.4955
	4	1.8938	10.4955
	5	1.071	128.5695
	6	1.1602	257.139
	7	0.7556	90.755
Inner Harbors	8	0.1153	234.7791
	9	0.005	46.9558
	10	0.0054	45.1876
	11	0.1288	88.5233
	12	0.0848	40.6009
Northern Entrance	13	0.0759	33.8553

Figure 4.16: Simulation 2, wave propagation from the south-east direction into Barcelona harbor, Hs=4.5 m , Tp=11 s. Significant wave height and peak period comparison.

Chapter 5

Conclusions

5.1 Summary

The open-source phase-resolving model REEF3D has been used for simulating unfavorable wave fields propagated into the Barcelona Harbor. This was used for the study of the wave field mainly focused on the area between "Muelle de la Energía" and "Muelle Prat", where the new dock has been projected. For the correct representation of the wave fields 3D and 2D simulations were carried out with different cell sizes over a $240km^2$ domain. Once convergence was reached on the 2D convergence study, simulations were carried out and analyzed. Three different simulations with different significant wave heights and peak periods, obtained from the coastal buoys were used to ensure the accuracy of the simulated wave fields. Thanks to the visual representation processed from Paraview non-linear phenomena such as diffraction and reflection could be analyzed, while MATLAB and Excel were used for the analysis of the significant wave heights and the spectral energy distribution on several locations of the harbor. Several conclusions were obtained, as well as suggestions for further work on harbor wave simulations.

5.2 Conclusions

The numerical phase-resolving numerical model REEF3D:FNPF is seen to be an effective solution for harbor and coastal modeling. Through the comparison of several simulations REEF3D:FNPF has shown to provide reliable and consistent results for modeling waves propagating from the coastal zone towards inner harbors. Therefore it can be considered an effective solution for wave studies for harbors as it captures wave transformations such as shoaling, energy dissipation, diffraction and reflection as well as significant wave height, peak period and spectral density distribution. The visual representation of such effects are key for their analysis and a valuable tool for

non-engineers to understand the effects of the topography and structures on waves. In regards to the Barcelona Harbor, their protection infrastructure has been shown to be effective as strong wave transformations occur and the significant wave height is reduced from a maximum of 4.8 meters observed on wave gauge 14 from simulation 1, to a maximum of 1.16 meters in the inner harbor, observed on wave gauge 6 from simulation 2, and the spectral energy is reduced from a maximum of $75.6m^2/Hz$ to $10.7m^2/Hz$ near the location where the new dock has been projected.

5.3 Suggestions for further harbor wave modeling

During the development of this thesis several problems were encountered, insufficient data for several harbors and the high computational demand to generate a 5 meter grid size domain for the 3D convergence study being the main ones. I have established several suggestions for future works on wave modeling in harbors with REEF3D.

Although the problem of insufficient data from the Barcelona was handled through a topographic survey done through Google Earth, I would considered it inefficient as the data was obtained on heterogeneous points around the dry ports perimeter. I believe that a set of homogeneous organized topographic data would have eased the development of the numerical domain. Regarding the challenge to generate a 5 meter grid size, I would suggest to reduce the domain size for the 3D convergence study in order to obtain conclusive results from inside the harbor, as the 2D convergence study was unable to consider the effects of the harbor on the domain. Lastly, although I have not considered it as a problem, I would suggest to set wave gauges closer to the generation zone and further offshore in order to analyze the correct generation of waves in the domain as well as other nonlinear phenomena such as whitecapping.

Bibliography

[1] A. Aggarwal, H. Bihs, D. Myrhaug, and M. Alagan Chella. Characteristics of breaking irregular wave forces on a monopile. *Applied Ocean Research*, 90:101846, 2019.

[2] A. Aggarwal, H. Bihs, S. Shirinov, and D. Myrhaug. Estimation of breaking wave properties and their interaction with a jacket structure. *Journal of Fluids and Structures*, 91:102722, 2019.

[3] M. Alagan Chella, H. Bihs, and D. Myrhaug. Wave impact pressure and kinematics due to breaking wave impingement on a monopile. *Journal of Fluids and Structures*, 86:94 – 123, 2019.

[4] A. Baquet, J. Kim, and Z. J. Huang. Numerical modeling using CFD and potential wave theory for three-hour nonlinear irregular wave simulations. In *International Conference on Offshore Mechanics and Arctic Engineering*, volume Volume 1: Offshore Technology, Trondheim, Norway, 06 2017.

[5] S. Beji and J. A. Battjes. Experimental investigation of wave propagation over a bar. *Coastal Engineering*, 19:151–162, 1993.

[6] H. Bihs, A. Kamath, M. Alagan Chella, A. Aggarwal, and Ø. A. Arntsen. A new level set numerical wave tank with improved density interpolation for complex wave hydrodynamics. *Computers & Fluids*, 140:191–208, 2016.

[7] H. Bihs, A. Kamath, M. Alagan Chella, A. Aggarwal, and Ø. A. Arntsen. A new level set numerical wave tank with improved density interpolation for complex wave hydrodynamics. *Computers & Fluids*, 140(Supplement C):191 – 208, 2016.

[8] H. Bihs, W. Wang, T. Martin, and A. Kamath. REEF3D::FNPF - A Flexible Fully Nonlinear Potential Flow Solver. In *Proceeding of 38th International Conference on Ocean, Offshore Arctic Engineering*, 2019.

[9] H. Bihs, W. Wang, T. Martin, and A. Kamath. REEF3D::FNPF - A Flexible Fully Nonlinear Potential Flow Solver. *Journal of Offshore Mechanics and Arctic Engineering*, 2020.

[10] H. Bihs, W. Wang, C. Pakozdi, and A. Kamath. Reef3d:: Fnpf—a flexible fully nonlinear potential flow solver. *Journal of Offshore Mechanics and Arctic Engineering*, 142(4), 2020.

[11] H. B. Bingham and H. Zhang. On the accuracy of finite-difference solutions for nonlinear water waves. *Journal of Engineering Mathematics*, pages 211–228, 2007.

[12] N. Booij, I. Haagsma, A. Kieftenburg, and L. Holthijsen. Swan implementation manual. *Delft University ofTechnology*, 2000.

[13] A. Brandt. Multi-level adaptive solutions to boundary-value problems. *Mathematics of computation*, 31(138):333–390, 1977.

[14] L. Cavaleri, J.-H. Alves, F. Ardhuin, A. Babanin, M. Banner, K. Belibassakis, M. Benoit, M. Donelan, J. Groeneweg, T. Herbers, et al. Wave modelling–the state of the art. *Progress in oceanography*, 75(4):603–674, 2007.

[15] D. Chalikov. Numerical modeling of sea waves. *Izvestiya, Atmospheric and Oceanic Physics*, 56(3):312–323, 2020.

[16] D. V. Chalikov. *Numerical modeling of sea waves*. Springer, 2016.

[17] A. Chorin. Numerical solution of the Navier-Stokes equations. *Mathematics of Computation*, 22:745–762, 1968.

[18] G. F. Clauss and W. L. Kühhnlein. Numerical Simulation of Nonlinear Transient Waves and its Validation by Laboratory Data. In *3rd International Conference on Fast Sea Transport*, volume 2, pages 1193–1204, Lubeck-Travemunde, Germany, 1995.

[19] J. S. A. do Carmo. Physical modelling vs. numerical modelling: complementarity and learning. 2020.

[20] G. Dwarakish and A. M. Salim. Review on the role of ports in the development of a nation. *Aquatic Procedia*, 124(7):295–301, 2015.

[21] Y. Eldeberky. Nonlinear effects in gravity waves propagating in shallow water. *Coastal Engineering Journal*, 54(04):1250024, 2012.

[22] A. Engsig-Karup and H. Bingham. Boundary-fitted solutions for 3d nonlinear water wave-structure interaction. In *IWWWFB24*, page 20, 2009.

[23] G. Z. Forristall. Wave crest distributions: Observations and second-order theory. *Journal of Physical Oceanography*, 30(8):1931–1943, 2000.

[24] C. J. Galvin Jr. Breaker type classification on three laboratory beaches. *Journal of geophysical research*, 73(12):3651–3659, 1968.

[25] K. Hasselmann. On the non-linear energy transfer in a gravity-wave spectrum part 1. general theory. *Journal of Fluid Mechanics*, 12(4):481–500, 1962.

[26] K. Hasselmann. On the spectral dissipation of ocean waves due to white capping. *Boundary-Layer Meteorology*, 6(1):107–127, 1974.

[27] C. Irribarren and C. Nogales. Protection des ports. In *XVII, International Navigation Congress, Section II, Comm*, volume 4, pages 27–47, 1949.

[28] N. G. Jacobsen, D. R. Fuhrman, and J. Fredsøe. A wave generation toolbox for the open-source CFD library: OpenFOAM. *International Journal for Numerical Methods in Fluids*, 70(9):1073–1088, 2012.

[29] A. Jeschke, G. K. Pedersen, S. Vater, and J. Behrens. Depth-averaged non-hydrostatic extension for shallow water equations with quadratic vertical pressure profile: equivalence to boussinesq-type equations. *International Journal for Numerical Methods in Fluids*, 84(10):569–583, 2017.

[30] G. S. Jiang and C. W. Shu. Efficient implementation of weighted ENO schemes. *Journal of Computational Physics*, 126:202–228, 1996.

[31] B. Li and C. A. Fleming. A three dimensional multigrid model for fully nonlinear water waves. *Coastal Engineering*, 1997.

[32] J. Liu, X.-T. Feng, X.-L. Ding, J. Zhang, and D.-M. Yue. Stability assessment of the three-gorges dam foundation, china, using physical and numerical modeling-part i: Physical model tests. *International Journal of Rock Mechanics and Mining Sciences*, 40:609–631, 07 2003.

[33] P. Madsen and O. Sørensen. Bound waves and triad interactions in shallow water. *Ocean Engineering*, 20(4):359–388, 1993.

[34] S. Mayer, A. Garapon, and L. S. Sørensen. A fractional step method for unsteady free surface flow with applications to non-linear wave dynamics. *International Journal for Numerical Methods in Fluids*, 28:293–315, 1998.

[35] S. Osher and J. A. Sethian. Fronts propagating with curvature-dependent speed: Algorithms based on Hamilton-Jacobi formulations. *Journal of Computational Physics*, 79:12–49, 1988.

[36] D. Peng, B. Merriman, S. Osher, H. Zhao, and M. Kang. A pde-based fast local level set method. *Journal of Computational Physics*, 155, 1999.

[37] Port Authority of Barcelona. Motor económico. http://www.portdebarcelona.cat/es/web/economic/inici, 2015. Accessed: 2018-08-30.

[38] Puertos del Estado. Predicción de oleaje, nivel del may; boyas y mareografos. http://www.puertos.es/es-es/oceanografia/Paginas/portus.aspx, 2019. Accessed: 2021-06-02.

[39] E. Quataert, C. Storlazzi, A. van Dongeren, and R. McCall. The importance of explicitly modelling sea-swell waves for runup on reef-lined coasts. *Coastal Engineering*, 160:103704, 2020.

[40] E. Rusu and C. G. Soares. Modeling waves in open coastal areas and harbors with phase-resolving and phase-averaged models. *Journal of Coastal Research*, 29(6):1309–1325, 2013.

[41] C. W. Shu and S. Osher. Efficient implementation of essentially non-oscillatory shock capturing schemes. *Journal of Computational Physics*, 77:439–471, 1988.

[42] H. Southgate. Review of wave breaking in shallow water. In *Wave Kinematics and Environmental Forces*. OnePetro, 1993.

[43] SWASH developers. SWASH User Manual version 4.01A. 2017.

[44] F. C. K. Ting and J. T. Kirby. Dynamics of surf-zone turbulence in a strong plunging breaker. *Coastal Engineering*, 24:177–204, 1995.

[45] B. Tovar, S. Jara-Diaz, and L. Trujillo. Econometric estimation of scale and scope economies within the port sector: a review. *Maritime Policy & Management*, 34(3):203–223, 2007.

[46] H. van der Vorst. BiCGStab: A fast and smoothly converging variant of Bi-CG for the solution of nonsymmetric linear systems. *SIAM Journal of Scientific Computing*, 13:631–644, 1992.

[47] S. Vold and A. E. Lothe. Mehamn - modellforsøk. Technical Report SBF IN F09203, SINTEF Byggforsk, Trondheim, June 2009.

[48] W. Wang. Large-scale phase-resolved wave modelling for the norwegian coast. 2020.

[49] W. Wang, T. Martin, A. Kamath, and H. Bihs. An improved depth-averaged non-hydrostatic shallow water model with quadratic pressure approximation. *International Journal for Numerical Methods in Fluids*, page 10.1002/fld.4807, 2020.

[50] W. Wang, T. Martin, A. Kamath, and H. Bihs. An improved depth-averaged nonhydrostatic shallow water model with quadratic pressure approximation. *International Journal for Numerical Methods in Fluids*, 92(8):803–824, 2020.

[51] I. R. Young. *Wind generated ocean waves*. Elsevier, 1999.

[52] M. Zijlema and G. Stelling. Efficient computation of surf zone waves using the nonlinear shallow water equations with non-hydrostatic pressure. *Coastal Engineering*, 55(10):780 – 790, 2008.

Chapter 6

Appendix

The contents of this appendix consist in all of the figures from the results of the simulations that have been carried out for the study of the waves in the harbor and the development of the thesis.

6.1 2D Convergence Study

The convergence study was carried out with an incident wave from the southeastern direction, a Hs=5.21 m and a Tp =10 s, with mesh sizes of 20, 10 5 and 8 meters. The spectrum of each wave gauge is represented in the following figures:

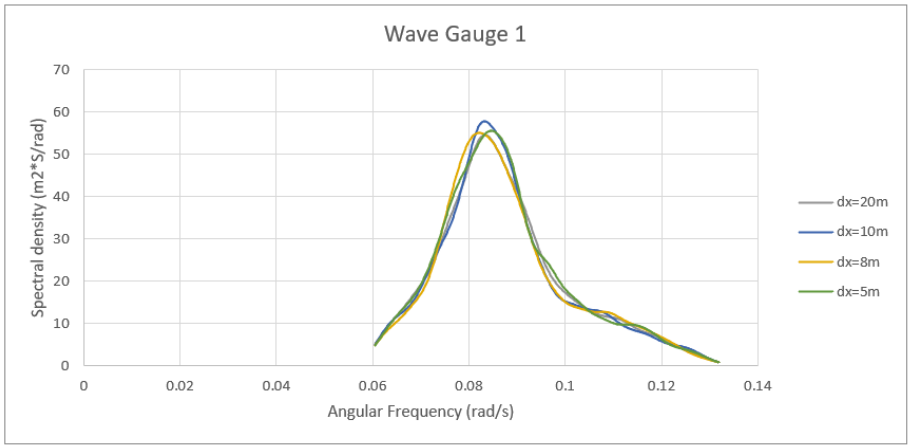

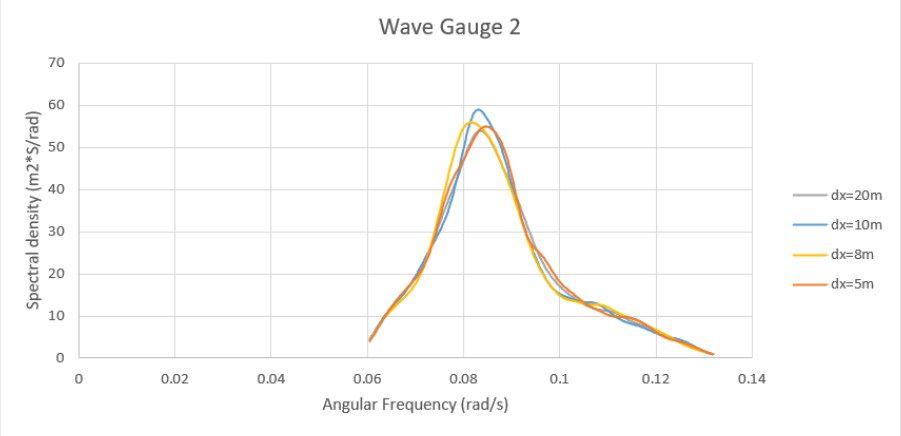
Wave Gauge 2
Spectral density (m2*S/rad)
Angular Frequency (rad/s)
dx=20m
dx=10m
dx=8m
dx=5m

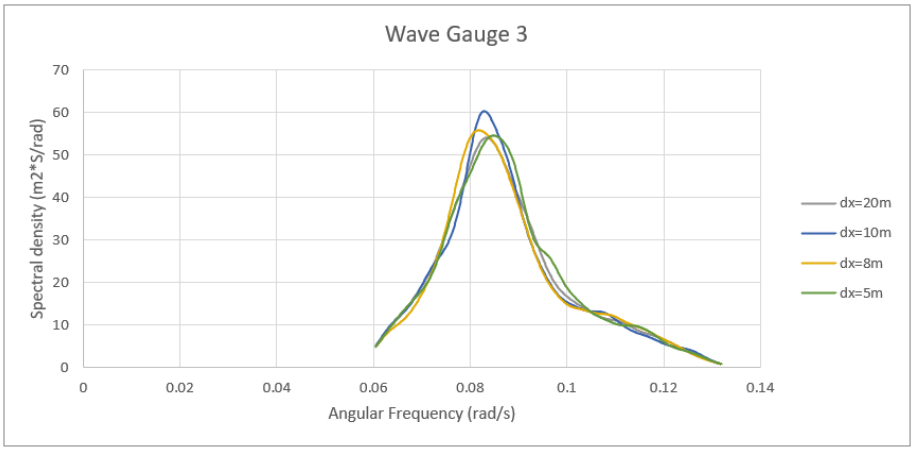
Wave Gauge 3
Spectral density (m2*S/rad)
Angular Frequency (rad/s)
dx=20m
dx=10m
dx=8m
dx=5m

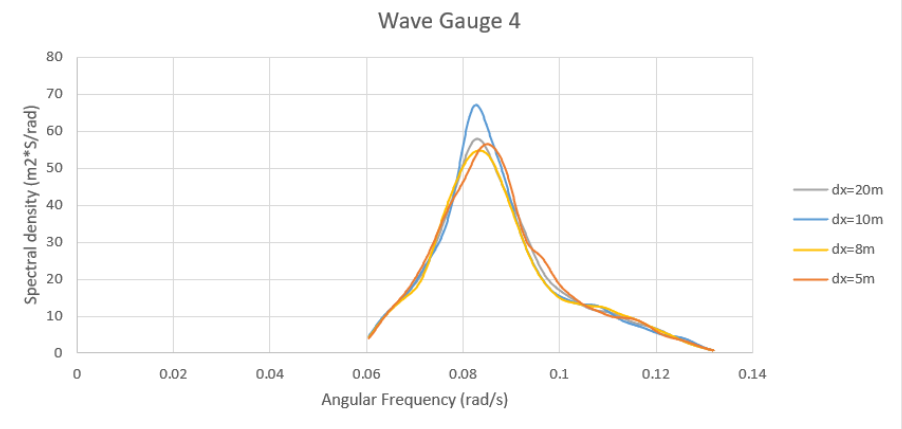
Wave Gauge 4
Spectral density (m2*S/rad)
Angular Frequency (rad/s)
dx=20m
dx=10m
dx=8m
dx=5m

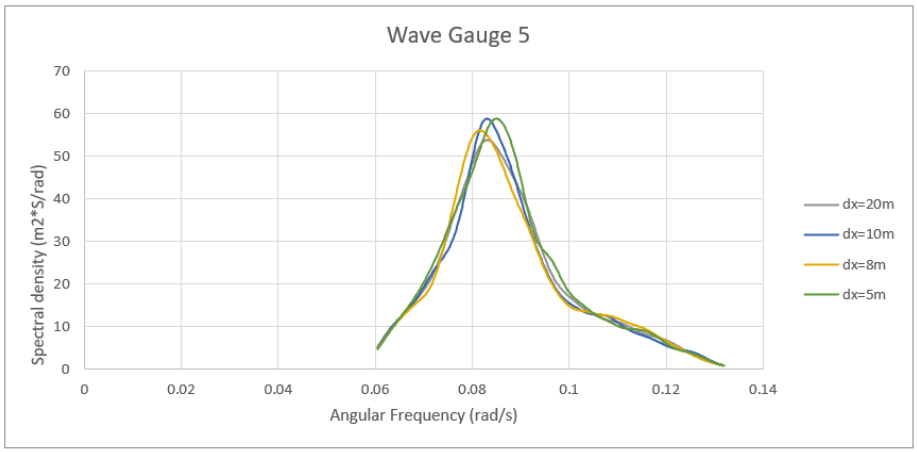
Wave Gauge 5
Spectral density (m2*S/rad)
Angular Frequency (rad/s)
dx=20m
dx=10m
dx=8m
dx=5m

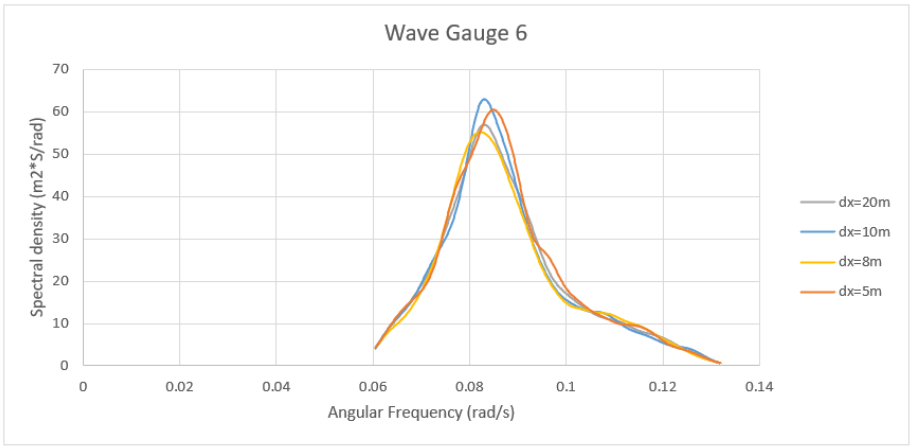
Wave Gauge 6
Spectral density (m2*S/rad)
Angular Frequency (rad/s)
dx=20m
dx=10m
dx=8m
dx=5m

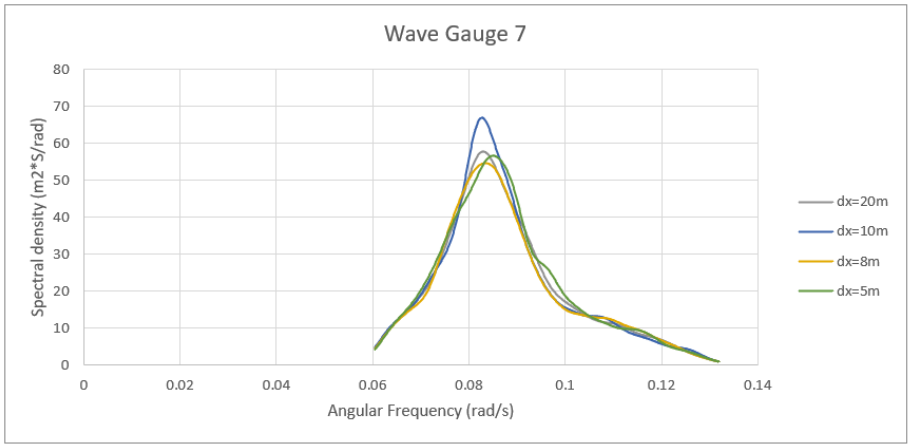
Wave Gauge 7
Spectral density (m2*S/rad)
Angular Frequency (rad/s)
dx=20m
dx=10m
dx=8m
dx=5m

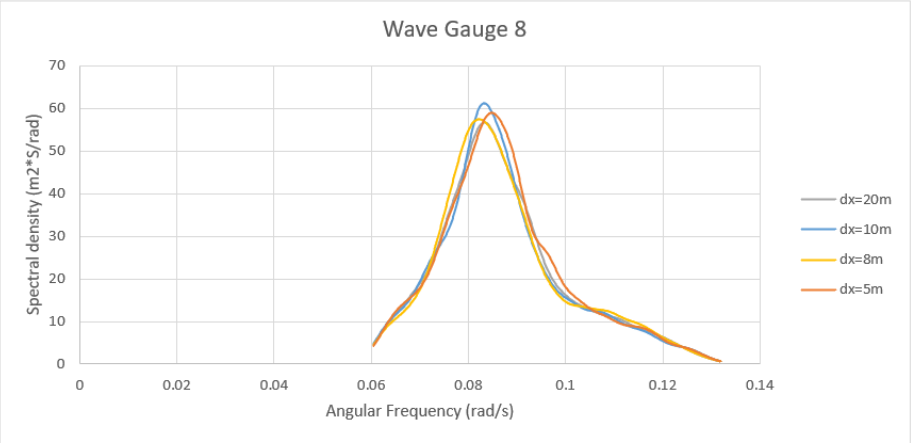
Wave Gauge 8
Spectral density (m2*S/rad)
Angular Frequency (rad/s)
dx=20m
dx=10m
dx=8m
dx=5m

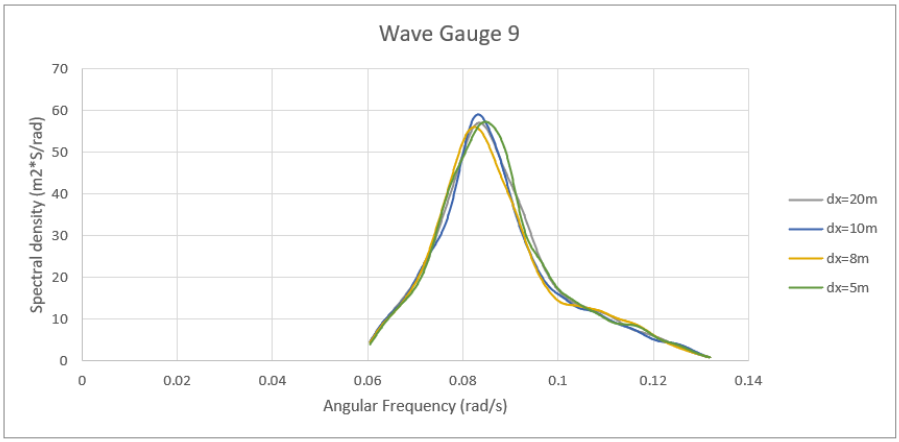
Wave Gauge 9
Spectral density (m2*S/rad)
Angular Frequency (rad/s)
dx=20m
dx=10m
dx=8m
dx=5m

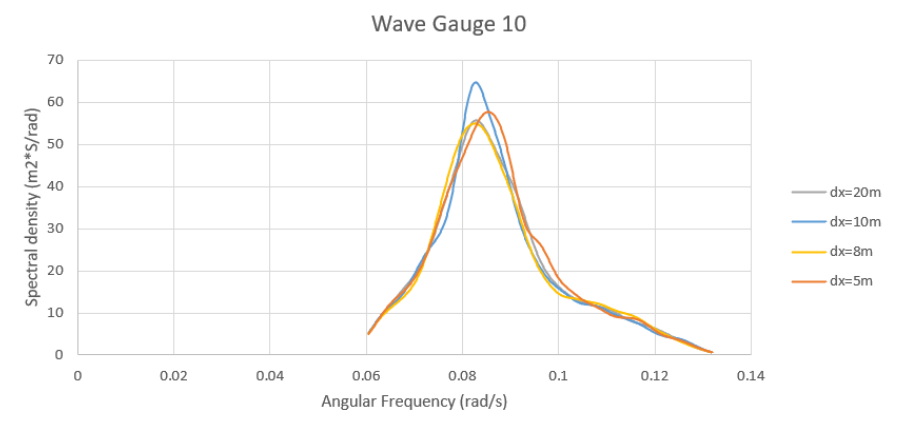
Wave Gauge 10
Spectral density (m2*S/rad)
Angular Frequency (rad/s)
dx=20m
dx=10m
dx=8m
dx=5m

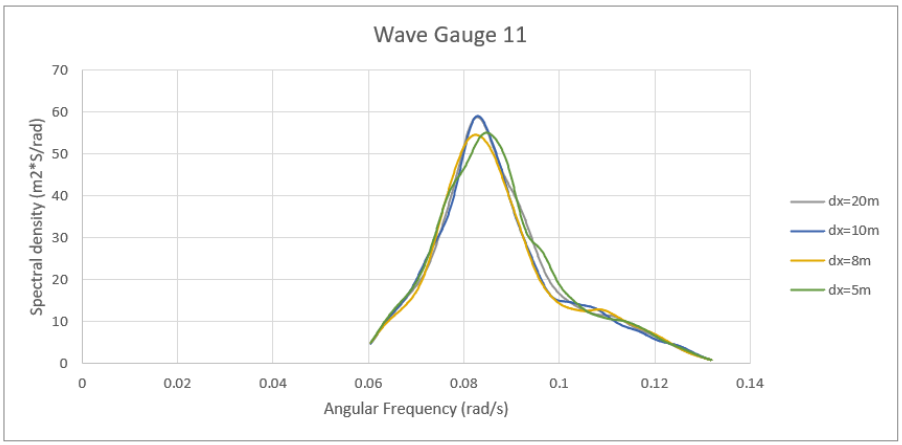
Wave Gauge 11
Spectral density (m2*S/rad)
70
60
50
40
30
20
10
0
0
0.02
0.04
0.06
0.08
0.1
0.12
0.14
Angular Frequency (rad/s)
dx=20m
dx=10m
dx=8m
dx=5m

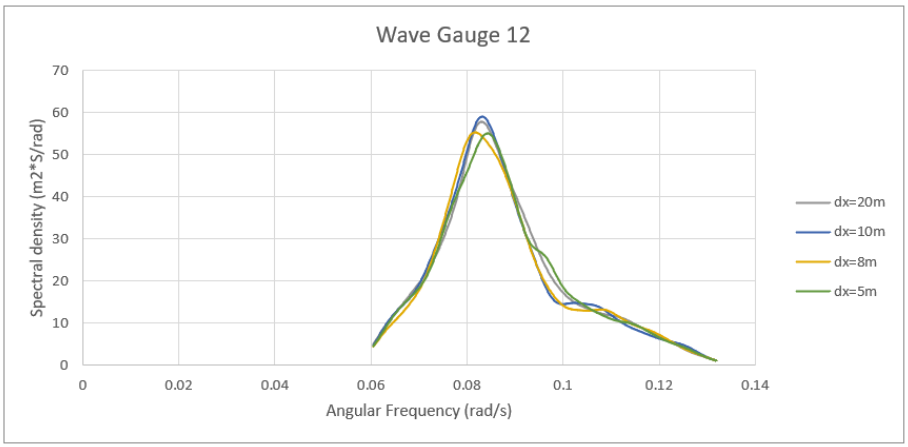
Wave Gauge 12
Spectral density (m2*S/rad)
70
60
50
40
30
20
10
0
0
0.02
0.04
0.06
0.08
0.1
0.12
0.14
Angular Frequency (rad/s)
dx=20m
dx=10m
dx=8m
dx=5m

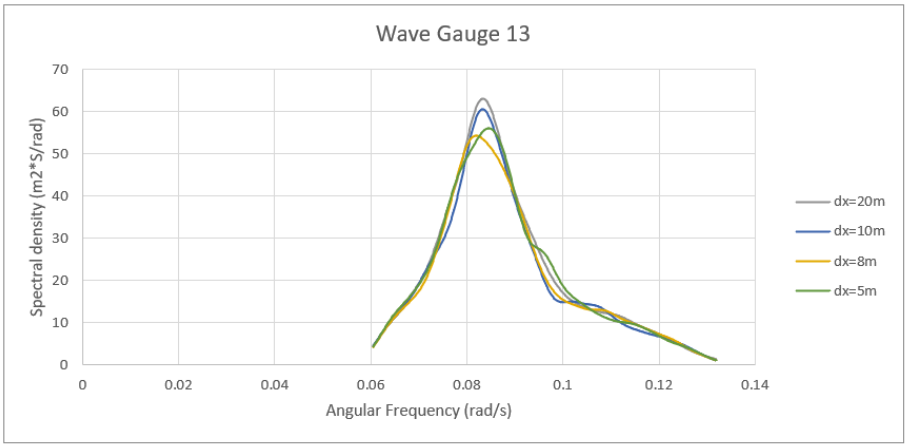
Wave Gauge 13
Spectral density (m2*S/rad)
70
60
50
40
30
20
10
0
0
0.02
0.04
0.06
0.08
0.1
0.12
0.14
Angular Frequency (rad/s)
dx=20m
dx=10m
dx=8m
dx=5m

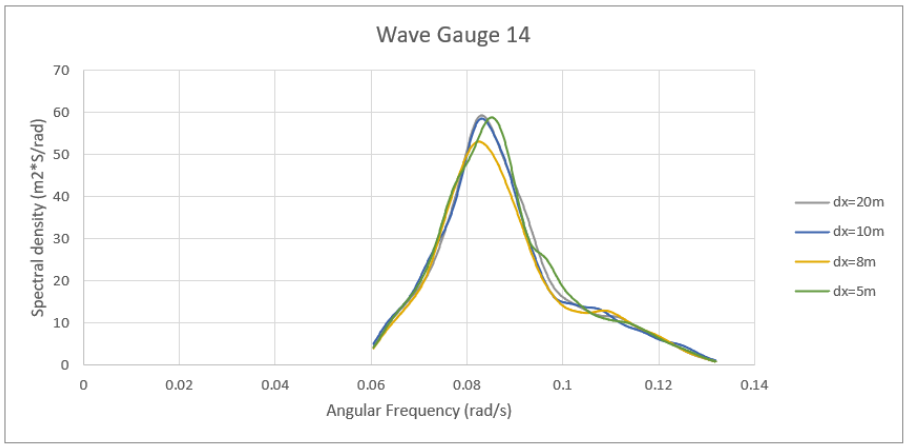
Wave Gauge 14
Spectral density (m2*S/rad)
Angular Frequency (rad/s)
dx=20m
dx=10m
dx=8m
dx=5m

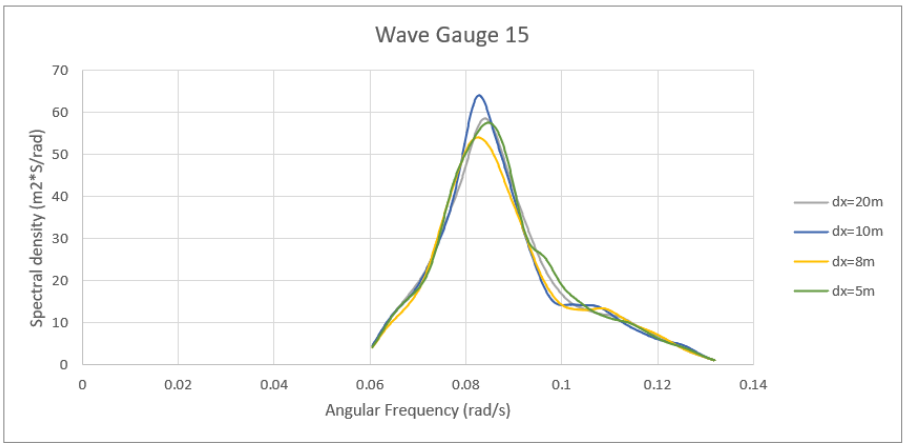
Wave Gauge 15
Spectral density (m2*S/rad)
Angular Frequency (rad/s)
dx=20m
dx=10m
dx=8m
dx=5m

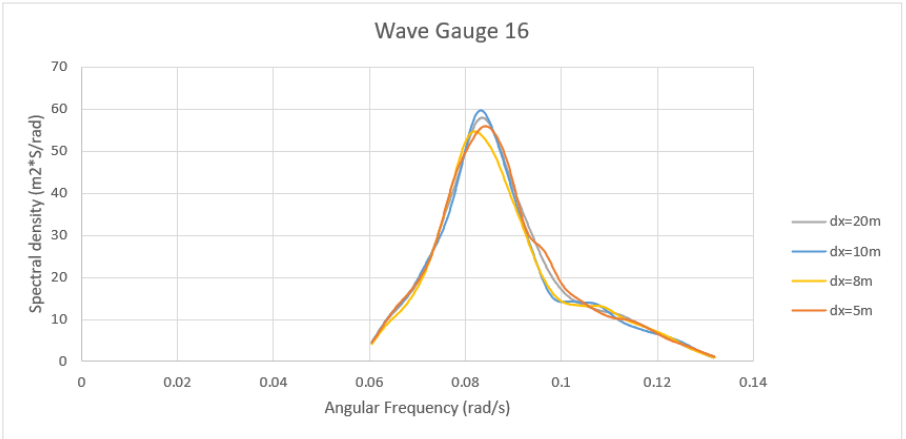
Wave Gauge 16
Spectral density (m2*S/rad)
Angular Frequency (rad/s)
dx=20m
dx=10m
dx=8m
dx=5m

6.2 3D Convergence Study

The 3D convergence study was made with an incident wave from the southeastern direction, a Hs=5.21m and a Tp=12s, with mesh sizes of 40, 20, 10 and 8 meters. 5 meter grid sizes were tried but are too computationally demanding. Although inconclusive results were obtained from this convergence study, there are some wave gauges were convergence is almost seen such as the following:

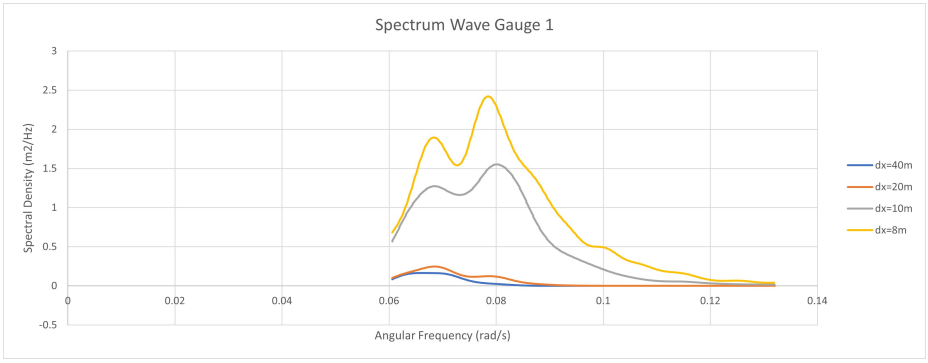

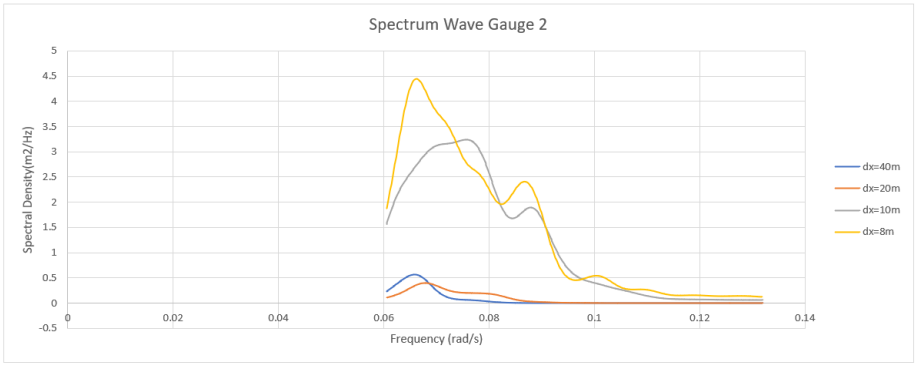

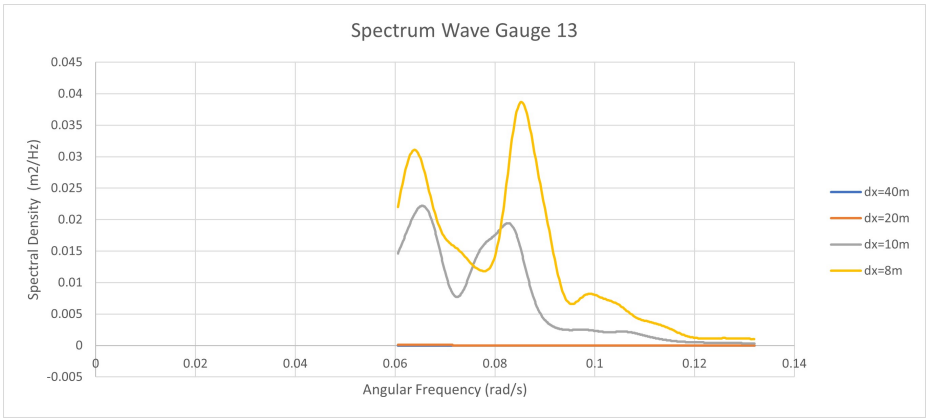

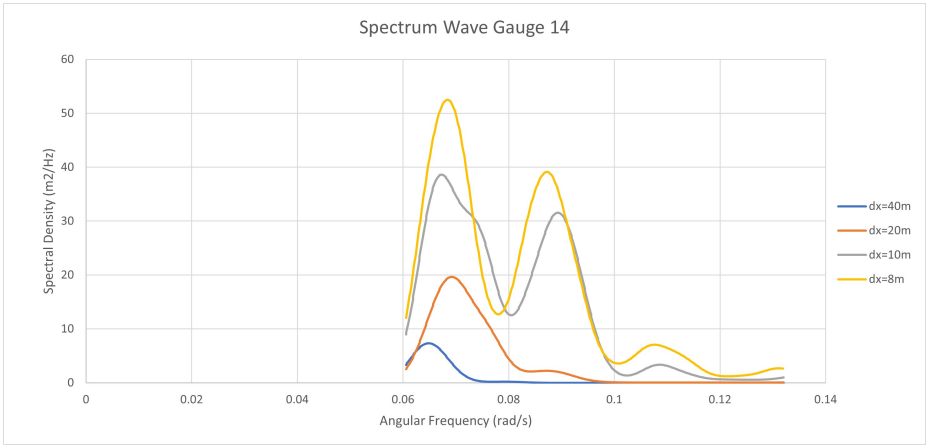

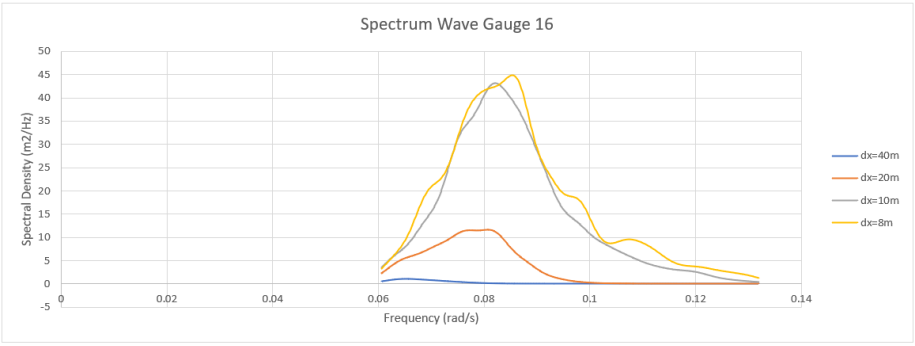

6.3 Simulation 1

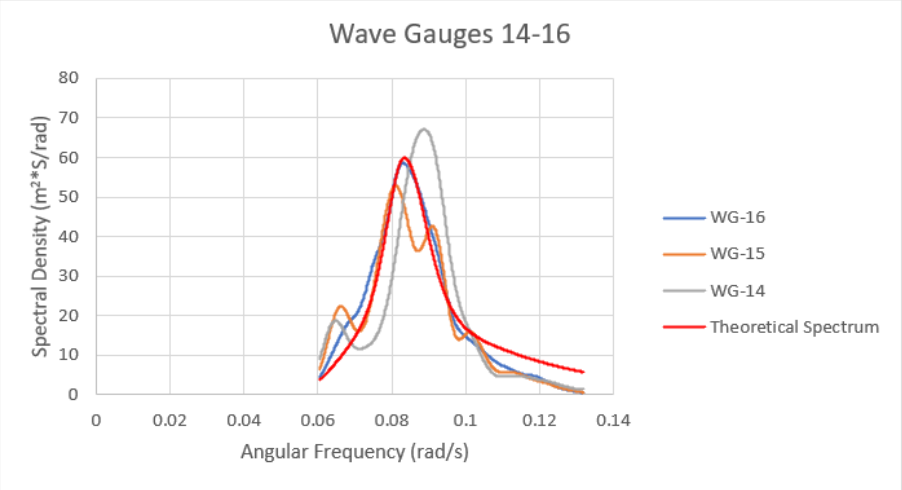

Figure 6.1: Simulation 1, wave propagation from the south-east direction into Barcelona harbor, Hs=5.21 m , Tp=12 s. Spectrum comparison at the southern entrance of the harbor. Concentration of energy from wave gauge 16 to 14 represents shoaling. Quadruplet and triad interactions can also be acknowledged as spectral density in wave the wave gauges are significantly higher than the theoretical spectrum.

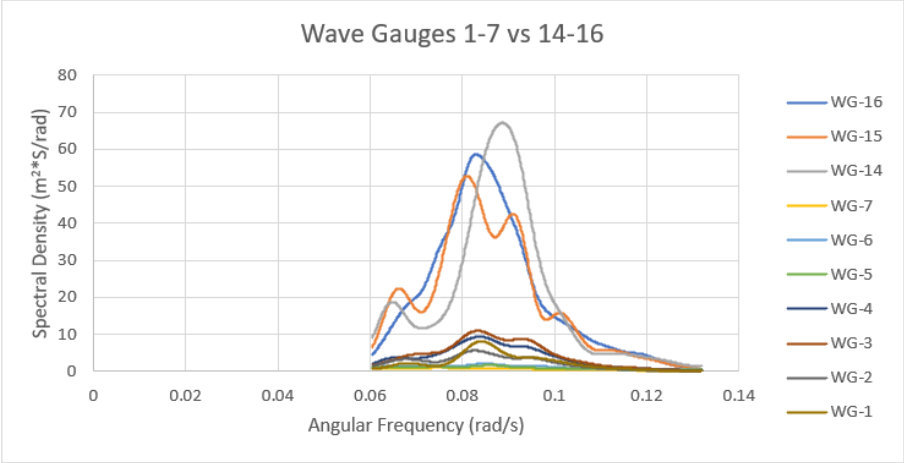

Figure 6.2: Simulation 1, wave propagation from the south-east direction into Barcelona harbor, Hs=5.21 m , Tp=12 s. Spectrum comparison between the southern entrance of the harbor and the main area of study. Loss of spectral density indicates wave breaking and energy dissipation.

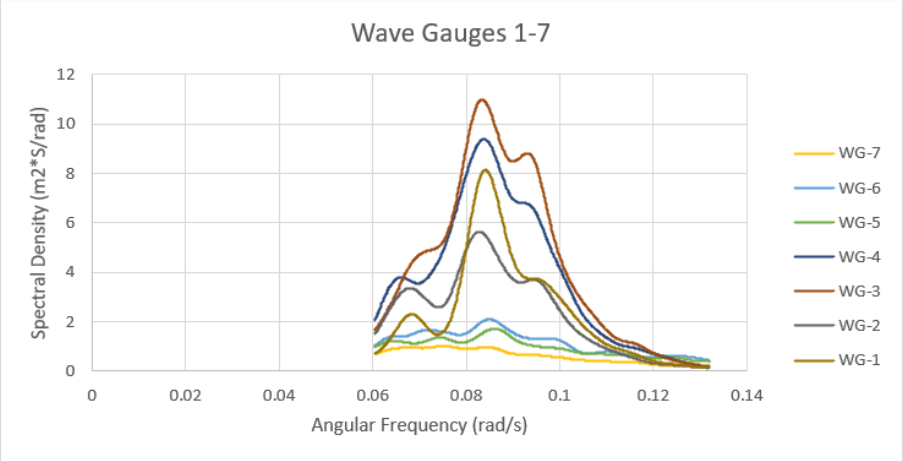

Figure 6.3: Simulation 1, wave propagation from the south-east direction into Barcelona harbor, Hs=5.21 m , Tp=12 s. Spectrum comparison at the main area of focus. Lower energy concentration can be seen at wave gauges 5, 6 and 7, the gauges closer to where the new dock has been projected. Several peaks can be seen in the spectrum, which represent the energy reflected by the harbor's infrastructure, south of the "Muelle Prat". We can observe that the angular frequency is fully represented as the minimum and maximum angular frequency of the forecast spectral densities concur with the theoretical spectrum.

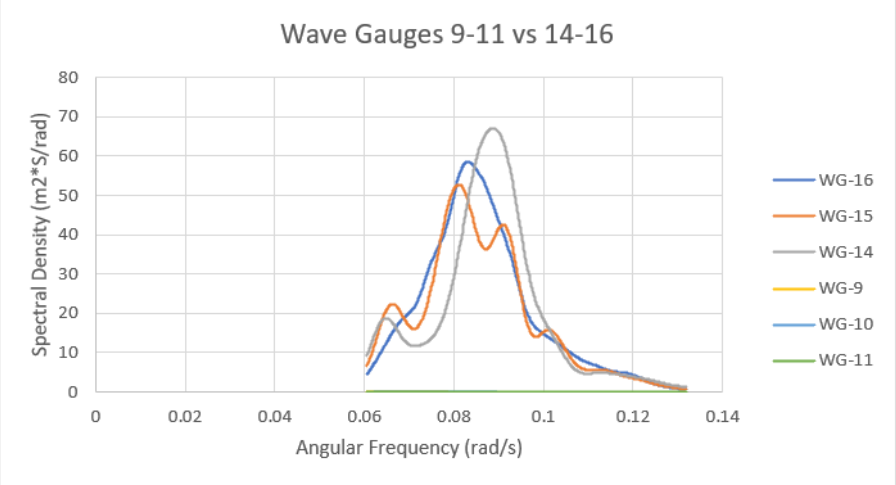

Figure 6.4: Simulation 1, wave propagation from the south-east direction into Barcelona harbor, Hs=5.21 m , Tp=12 s. Spectrum comparison between southern entrance and inner harbor. A significant reduction of energy density can be seen which indicates the effectiveness of the harbor's protection infrastructure, reducing the spectral energy from a maximum of $67m^2/Hz$ on wave gauge 14 to a maximum of $0.08m^2/Hz$ on wave gauge 11.

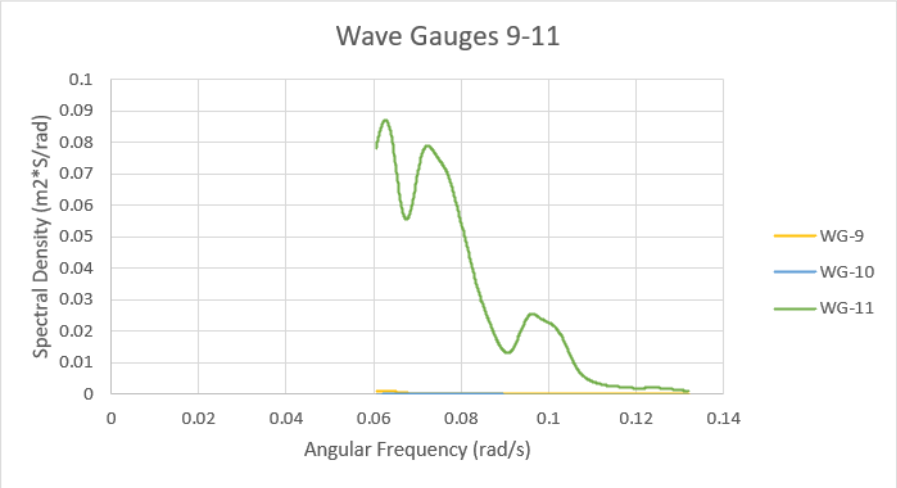

Figure 6.5: Simulation 1, wave propagation from the south-east direction into Barcelona harbor, Hs=5.21 m , Tp=12 s. Spectrum comparison between wave gauges in inner harbors. Three peaks of energy can be seen in wave gauge 11 which indicates the effects of reflection. This wave transformation seems to prevent entrance to the energy in the inner harbor as spectral density is under $0.001 m^2/Hz$ in wave gauges 9 and 10.

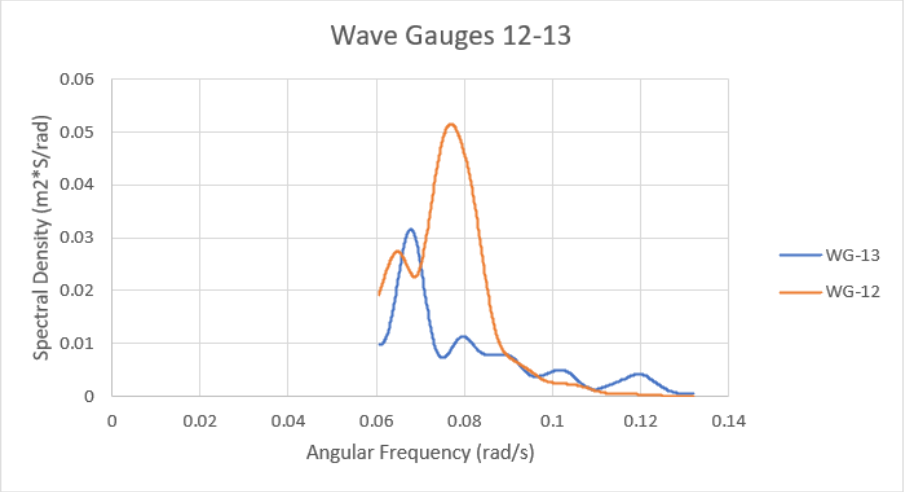

Figure 6.6: Simulation 1, wave propagation from the south-east direction into Barcelona harbor, Hs=5.21 m , Tp=12 s. Spectrum comparison between northern entrance and inner harbor. A significant reduction of energy density can be seen which indicates the effectiveness of the harbor's protection infrastructure. As well as several peaks of energy with indicate both the presence of diffraction and reflected waves.

SE_1			
Location	WG	Hs	Tp
Southern Entrance	16	4.8031	11.5137
	15	4.6404	12.6759
	14	4.7989	11.009
Area of Focus	1	1.6583	257.139
	2	1.6254	257.139
	3	2.2223	10.5262
	4	2.071	10.5262
	5	1.0497	98.1804
	6	1.1534	257.139
	7	0.843	257.139
Inner Harbors	8	0.1373	234.7791
	9	0.0108	46.7526
	10	0.0075	44.9993
	11	0.182	88.5233
	12	0.1247	33.7495
Northern Entrance	13	0.0929	29.9996

Figure 6.7: Simulation 1, wave propagation from the south-east direction into Barcelona harbor, Hs=5.21 m , Tp=12 s. Significant wave height and peak period comparison in the different regions of the harbor's basin.

Figure 6.8: Simulation 1, wave propagation from the south-east direction into Barcelona harbor, Hs=5.21 m , Tp=12 s. Irregular waves generated from the left boundary. The effects of the changing bathymetry can be seen as waves are refracted while propagating towards shore.

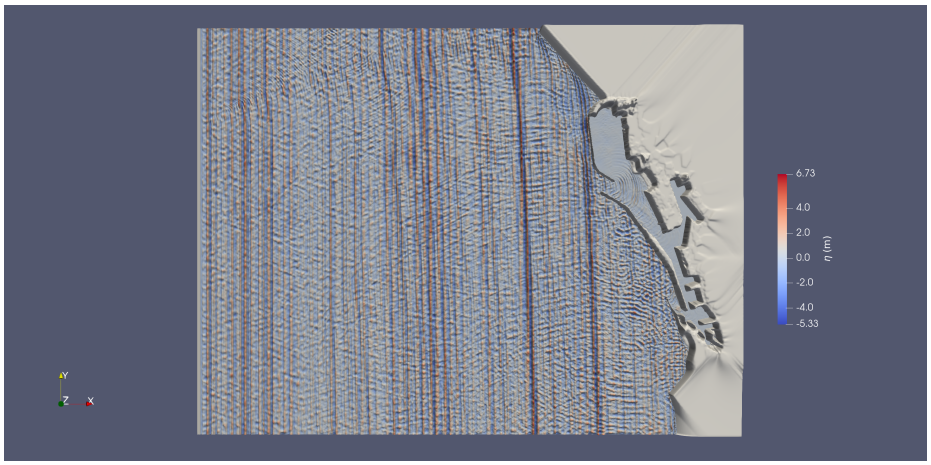

Figure 6.9: Simulation 1, wave propagation from the south-east direction into Barcelona harbor, Hs=5.21 m , Tp=12 s. Irregular waves propagated throughout the entire domain.

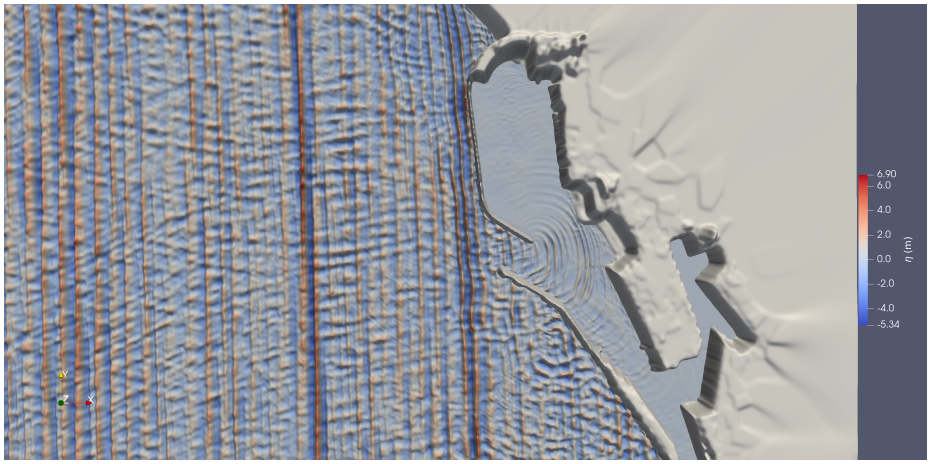

Figure 6.10: Simulation 1, wave propagation from the south-east direction into Barcelona harbor, Hs=5.21 m , Tp=12 s. Irregular waves propagated throughout the entire domain, focused on the main area of study.

6.4 Simulation 2

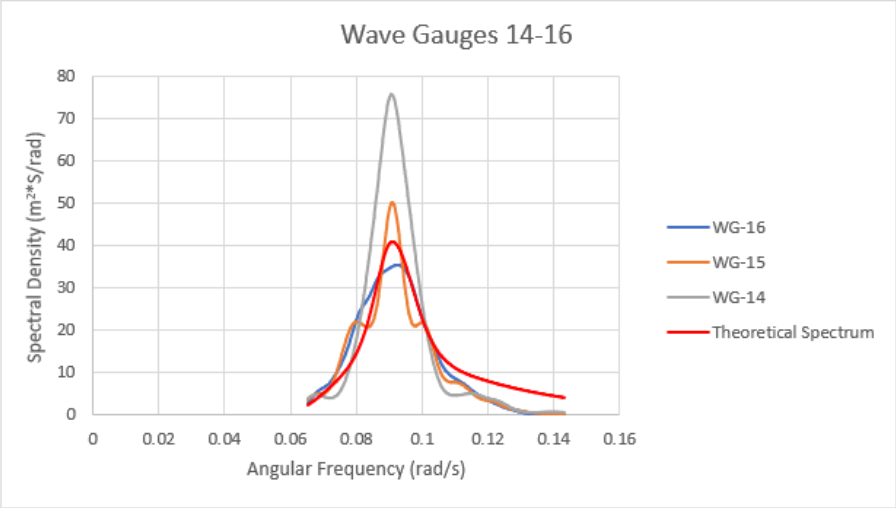

Figure 6.11: Simulation 2, wave propagation from the south-east direction into Barcelona harbor, Hs=4.5 m , Tp=11 s. Spectrum comparison at the southern entrance of the harbor. Concentration of energy from wave gauge 16 to 14 represents shoaling. Quadruplet and triad interactions can also be acknowledged as spectral density in wave the wave gauges are significantly higher than the theoretical spectrum.

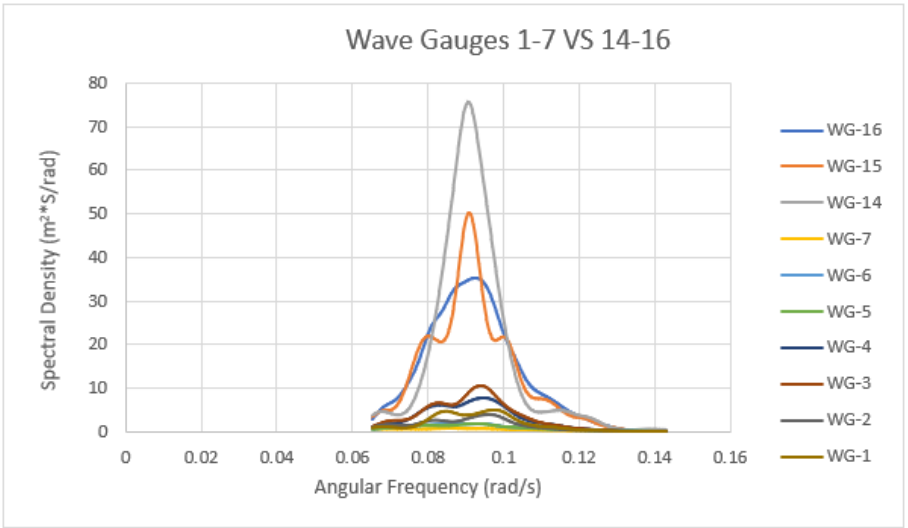

Figure 6.12: Simulation 2, wave propagation from the south-east direction into Barcelona harbor, Hs=4.5 m , Tp=11 s. Spectrum comparison between the southern entrance of the harbor and the main area of study. Loss of spectral density indicates wave breaking and energy dissipation.

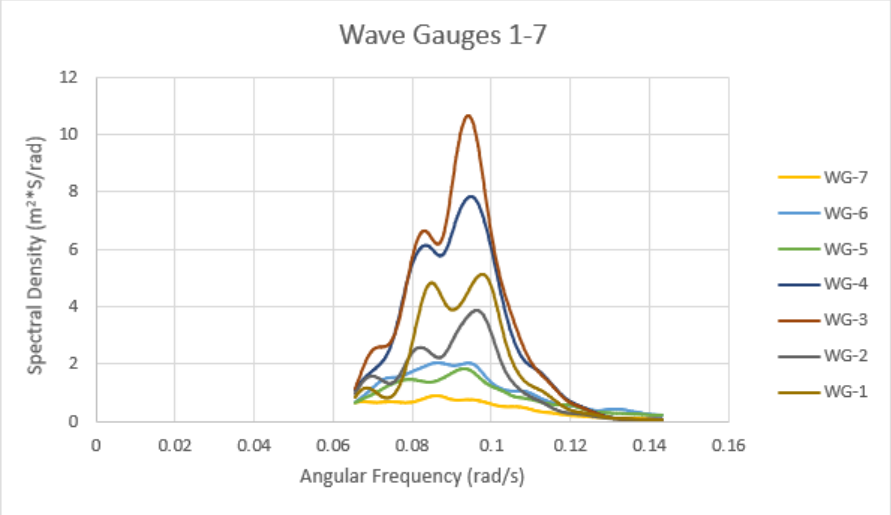

Figure 6.13: Simulation 2, wave propagation from the south-east direction into Barcelona harbor, Hs=4.5 m , Tp=11 s. Spectrum comparison at the main area of focus. Lower energy concentration can be seen at wave gauges 5, 6 and 7, the gauges closer to where the new dock has been projected. Several peaks can be seen in the spectrum, which represent the energy reflected by the harbor's infrastructure, south of the "Muelle Prat". We can observe that the angular frequency is fully represented as the minimum and maximum angular frequency of the forecast spectral densities concur with the theoretical spectrum.

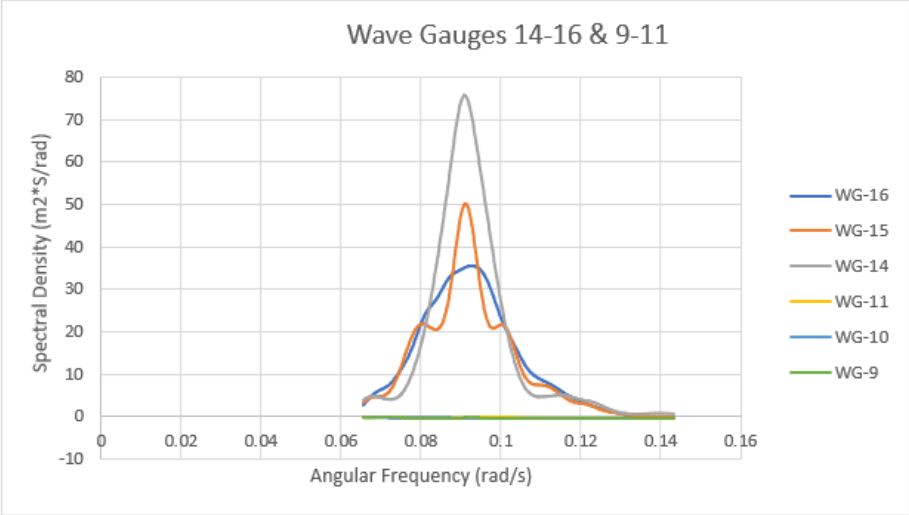

Figure 6.14: Simulation 2, wave propagation from the south-east direction into Barcelona harbor, Hs=5.21 m , Tp=12 s. Spectrum comparison between southern entrance and inner harbor. A significant reduction of energy density can be seen which indicates the effectiveness of the harbor's protection infrastructure, reducing the spectral energy from a maximum of $75m^2/Hz$ on wave gauge 14 to a maximum of $0.04m^2/Hz$ on wave gauge 11.

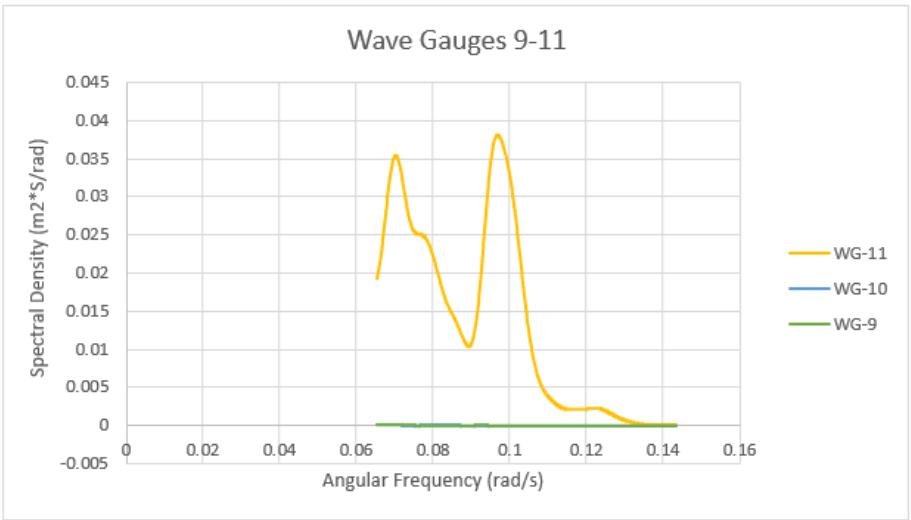

Figure 6.15: Simulation 2, wave propagation from the south-east direction into Barcelona harbor, Hs=4.5 m , Tp=12 s. Spectrum comparison between wave gauges in inner harbors. Three peaks of energy can be seen in wave gauge 11 which indicates the effects of reflection. This wave transformation seems to prevent entrance to the energy in the inner harbor as spectral density is under $0.001m^2/Hz$ in wave gauges 9 and 10.

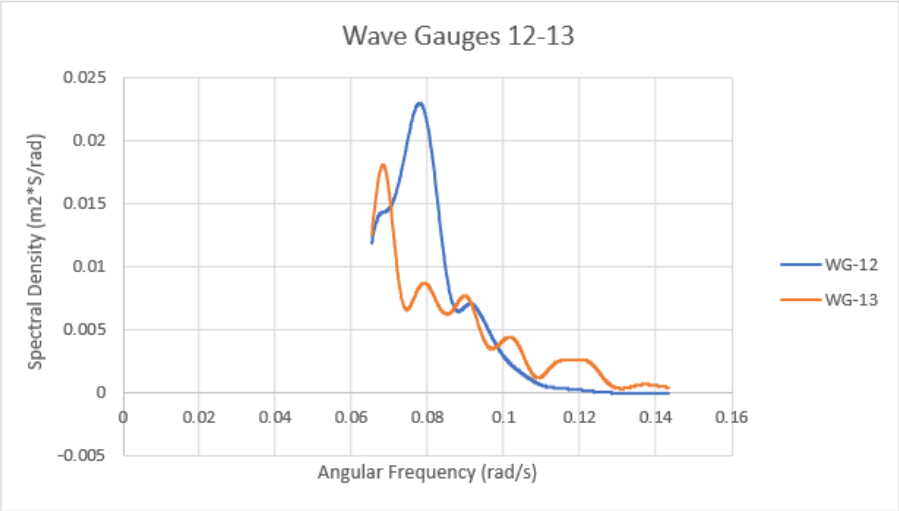

Figure 6.16: Simulation 2, wave propagation from the south-east direction into Barcelona harbor, Hs=4.5 m , Tp=11 s. Spectrum comparison between northern entrance and inner harbor. A significant reduction of energy density can be seen which indicates the effectiveness of the harbor's protection infrastructure. As well as several peaks of energy with indicate both the presence of diffraction and reflected waves.

SE_2			
Location	WG	Hs	Tp
Southern Entrance	16	3.9791	10.8869
	15	3.9096	11.0995
	14	4.5173	10.4955
Area of Focus	1	1.5031	10.4955
	2	1.2927	257.139
	3	2.0371	10.4955
	4	1.8938	10.4955
	5	1.071	128.5695
	6	1.1602	257.139
	7	0.7556	90.755
Inner Harbors	8	0.1153	234.7791
	9	0.005	46.9558
	10	0.0054	45.1876
	11	0.1288	88.5233
	12	0.0848	40.6009
Northern Entrance	13	0.0759	33.8553

Figure 6.17: Simulation 2, wave propagation from the south-east direction into Barcelona harbor, Hs=4.5 m , Tp=11 s. Significant wave height and peak period comparison in the different regions of the harbor's basin.

Figure 6.18: Simulation 1, wave propagation from the south-east direction into Barcelona harbor, Hs=4.5 m , Tp=11 s. Irregular waves generated from the left boundary.

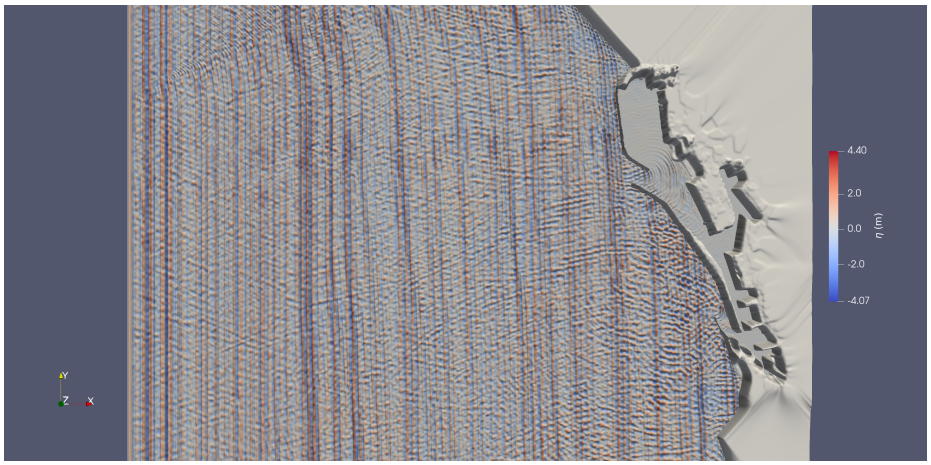

Figure 6.19: Simulation 2, wave propagation from the south-east direction into Barcelona harbor, Hs=4.5 m , Tp=10 s. Irregular waves propagated throughout the entire domain.

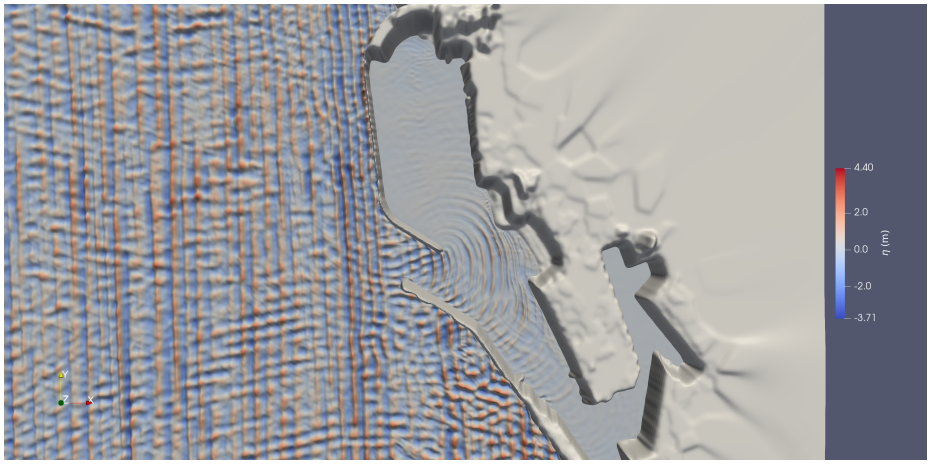

Figure 6.20: Simulation 2, wave propagation from the south-east direction into Barcelona harbor, Hs=4.5 m , Tp=10 s. Irregular waves propagated throughout the entire domain, focused on the main area of study.

6.5 Simulation 3

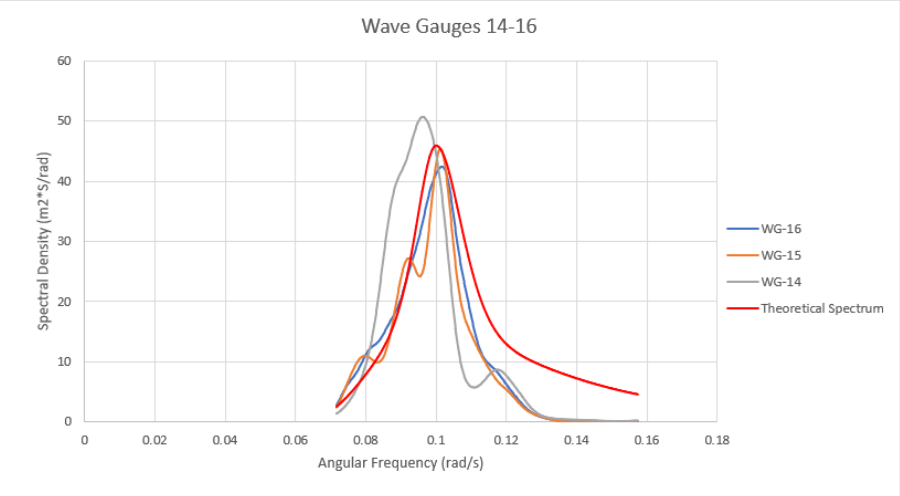

Figure 6.21: Simulation 3, wave propagation from the south-east direction into Barcelona harbor, Hs=5.0 m , Tp=10 s. Spectrum comparison at the southern entrance of the harbor. Concentration of energy from wave gauge 16 to 14 represents shoaling. Quadruplet and triad interactions can also be acknowledged as spectral density in wave the wave gauges are significantly higher than the theoretical spectrum.

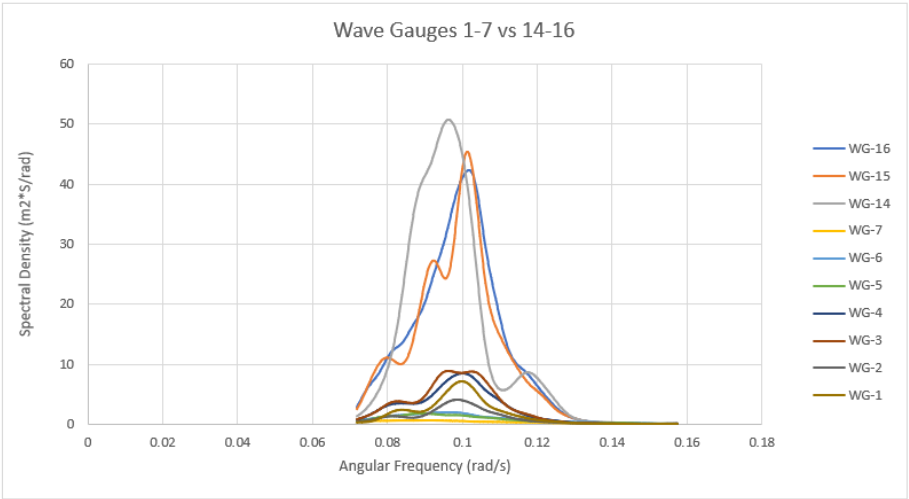

Figure 6.22: Simulation 3, wave propagation from the south-east direction into Barcelona harbor, Hs=5.0 m , Tp=10 s. Spectrum comparison between the southern entrance of the harbor and the main area of study. Loss of spectral density indicates wave breaking and energy dissipation.

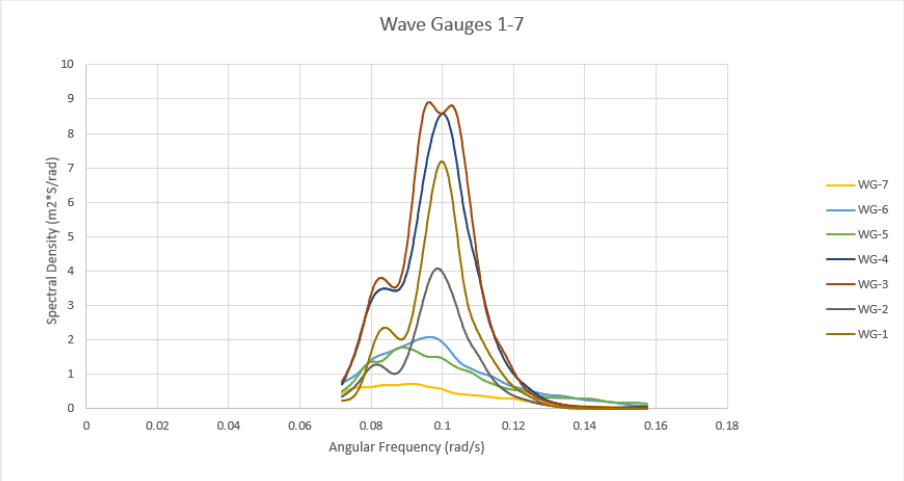

Figure 6.23: Simulation 3, wave propagation from the south-east direction into Barcelona harbor, Hs=5.0 m , Tp=10 s. Spectrum comparison at the main area of focus. Lower energy concentration can be seen at wave gauges 5, 6 and 7, the gauges closer to where the new dock has been projected. Several peaks can be seen in the spectrum, which represent the energy reflected by the harbor's infrastructure, south of the "Muelle Prat". We can observe that the angular frequency is fully represented as the minimum and maximum angular frequency of the forecast spectral densities concur with the theoretical spectrum.

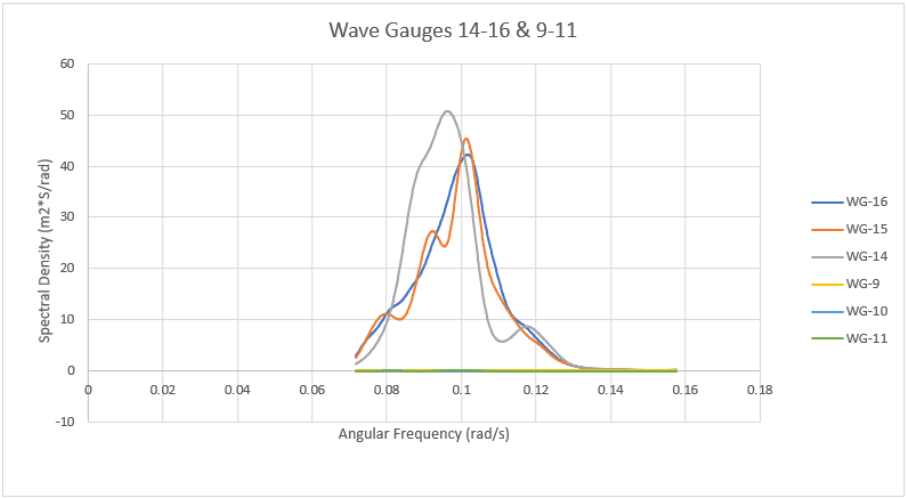

Figure 6.24: Simulation 3, wave propagation from the south-east direction into Barcelona harbor, Hs=5.0 m , Tp=10 s. Spectrum comparison between southern entrance and inner harbor. A significant reduction of energy density can be seen which indicates the effectiveness of the harbor's protection infrastructure, reducing the spectral energy from a maximum of $51m^2/Hz$ on wave gauge 14 to a maximum of $0.06m^2/Hz$ on wave gauge 11.

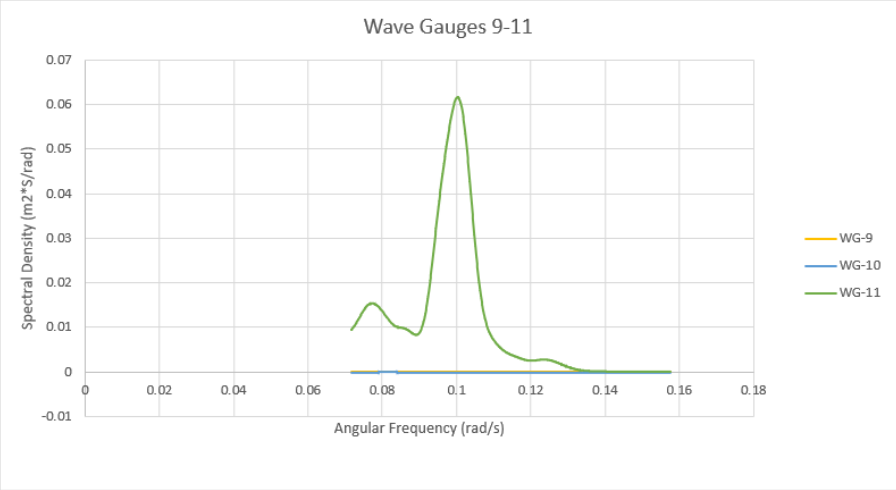

Figure 6.25: Simulation 3, wave propagation from the south-east direction into Barcelona harbor, Hs=5.0 m , Tp=10 s. Spectrum comparison between wave gauges in inner harbors. Three peaks of energy can be seen in wave gauge 11 which indicates the effects of reflection. This wave transformation seems to prevent entrance to the energy in the inner harbor as spectral density is under $0.001 m^2/Hz$ in wave gauges 9 and 10.

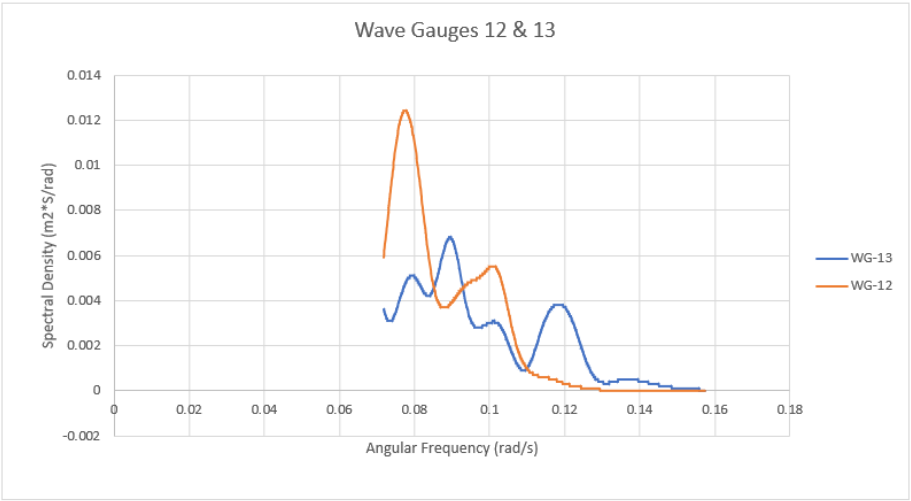

Figure 6.26: Simulation 3, wave propagation from the south-east direction into Barcelona harbor, Hs=5.0 m , Tp=10 s. Spectrum comparison between northern entrance and inner harbor. A significant reduction of energy density can be seen which indicates the effectiveness of the harbor's protection infrastructure. As well as several peaks of energy with indicate both the presence of diffraction and reflected waves.

SE_3			
Location	WG	Hs	Tp
Southern Entrance	16	3.9638	11.3206
	15	3.8151	9.8629
	14	4.2092	9.7121
Area of Focus	1	1.4891	10.1693
	2	1.1842	257.139
	3	1.932	257.139
	4	1.8319	10.1693
	5	1.0549	99.9985
	6	1.1246	257.139
	7	0.6956	257.139
Inner Harbors	8	0.1047	229.7838
	9	0.0029	46.3512
	10	0.0035	45.3775
	11	0.1236	121.3465
	12	0.0613	41.2208
Northern Entrance	13	0.0564	26.7986

Figure 6.27: Simulation 3, wave propagation from the south-east direction into Barcelona harbor, Hs=5.0 m , Tp=10 s. Significant wave height and peak period comparison in the different regions of the harbor's basin.

Figure 6.28: Simulation 3, wave propagation from the south-east direction into Barcelona harbor, Hs=5.0 m , Tp=10 s. Irregular waves generated from the left boundary. Refraction can be seen as waves propagate near shore.

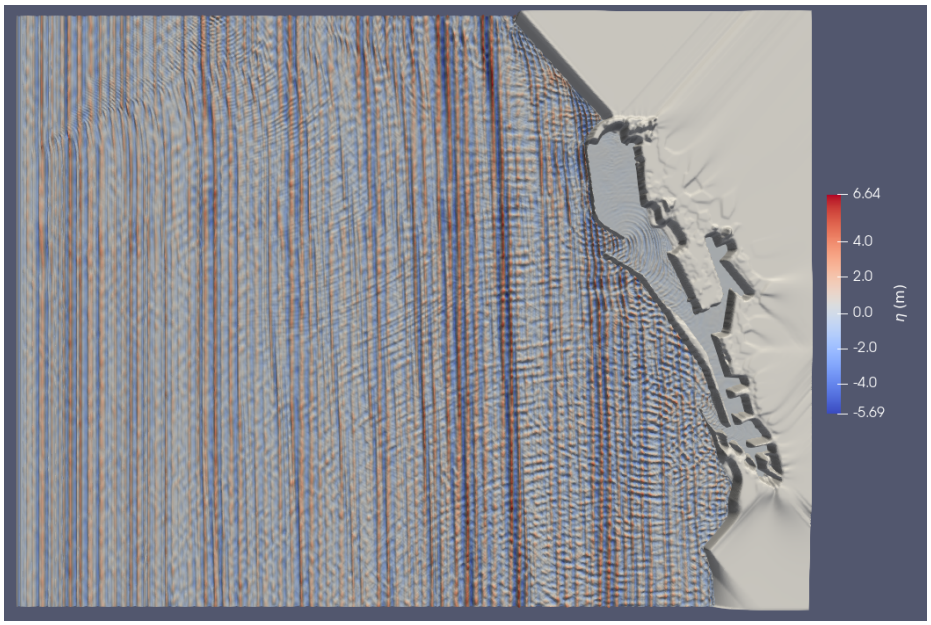

Figure 6.29: Simulation 3, wave propagation from the south-east direction into Barcelona harbor, Hs=5.0 m, Tp=10 s. Irregular waves propagated throughout the entire domain.

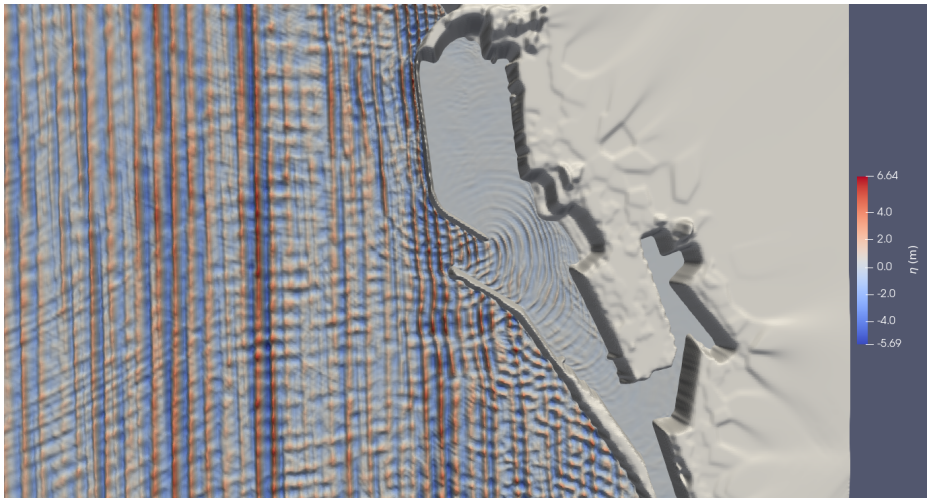

Figure 6.30: Simulation 3, wave propagation from the south-east direction into Barcelona harbor, Hs=5.0 m , Tp=10 s. Irregular waves propagated throughout the entire domain, focused on the main area of study.